MCD *C*-Term Signs, Saturation Behavior, and Determination of Band Polarizations in Randomly Oriented Systems with Spin $S \geq {}^1/_2$. Applications to $S = {}^1/_2$ and $S = {}^5/_2$

Frank Neese and Edward I. Solomon*

Department of Chemistry, Stanford University, Stanford, California 94305

Received October 29, 1998

The magnetic circular dichroism (MCD) properties of a spin-allowed transition from an orbitally nondegenerate ground state manifold *A* to an orbitally nondegenerate excited state manifold *J* in the presence of spin−orbit coupling (SOC) are derived for any $S \geq {}^1/_2$. Three physically distinct mechanisms are identified that lead to MCD intensity and depend on SOC between excited states which leads to a sum rule and SOC between the ground state and other excited states that leads to deviations from the sum rule. The model is valid for any symmetry of the magnetic coupling tensors and arbitrary transition polarizations. The $S = {}^1/_2$ case is analytically solved, and the determination of linear polarizations from MCD saturation magnetization data is discussed. For all mechanisms the MCD intensity is proportional to the spin-expectation values of the ground state sublevels which are conveniently generated from a spin-Hamiltonian (SH). For Kramers systems with large zero-field splittings (ZFSs) this allows the contribution from each Kramers doublet to the total MCD intensity to be related through their effective *g*-values, therefore significantly reducing the number of parameters required to analyze experimental data. The behavior of high-spin systems is discussed in the limits of weak, intermediate, and strong ZFS relative to the Zeeman energy. The model remains valid in the important case of intermediate ZFS where the ground state sublevels may cross as a function of applied magnetic field and there are significant off-axis contributions to the MCD intensity due to a change of the electron spin quantization axis. The model permits calculation of MCD *C*-term signs from molecular wave functions, and explicit expressions are derived in terms of MOs for $S = {}^1/_2$ and $S = {}^5/_2$. Two examples from the literature are analyzed to demonstrate how the *C*-term signs can be evaluated by a graphical method that gives insight into their physical origin.

1. Introduction

Magnetic circular dichroism (MCD) has become an important experimental technique for the investigation of the geometric and electronic structures of transition metal complexes in a variety of areas, perhaps most notably bioinorganic chemistry.[1,2] In an MCD experiment one measures the differential absorption of left and right circularly polarized light induced in the presence of a longitudinal magnetic field. MCD has several features that make it a particularly attractive spectroscopic tool. (a) It is a sensitive technique especially in the near-IR (NR) region where it is difficult to observe absorption bands in aqueous solutions of metalloproteins. (b) It is site selective. In a system with several chromophores that have distinct absorption bands, individual centers can be studied. (c) MCD is multidimensional. Experimental variables are the temperature that can be accurately controlled from 1.5 K to room temperature, the magnetic field up to about 10 T, and the wavelength of the incident radiation. (d) This technique does not require expensive isotopic enrichments and is not restricted to iron-containing compounds in contrast to Mössbauer spectroscopy. (e) MCD permits investigation of even-electron non-Kramers systems that are frequently difficult to study with EPR and related techniques. (f) The spectrum is a signed quantity and therefore usually offers much higher resolution than absorption spectroscopy particularly in regions of overlapping absorption bands. (g) MCD simultaneously provides information about the ground and the excited states of the species under study and is therefore an invaluable link between techniques like EPR, which primarily probe the electronic ground state, and absorption or resonance Raman spectroscopy, which primarily probe electronically excited states.[3] (h) From a theoretical point of view, calculation of MCD parameters involves combinations of matrix elements that are different from other techniques and therefore puts constraints on electronic structure models for transition metal complexes. It can therefore allow rigorous spectral assignments. (i) MCD (like ENDOR) provides orientational selectivity even for a frozen solution. Due to the sensitivity of the MCD intensity to the transition polarizations, only a subset of randomly oriented molecules contributes to a given MCD signal.

* Author to whom correspondence should be addressed.

(1) (a) Dooley, D. M.; Dawson, J. H. *Coord. Chem. Rev.* **1984**, *60*, 1. (b) Thomson, A. J.; Cheesman, M. R.; George, S. K. *Methods Enzymol.* **1993**, *226*, 199. (c) Cheesman, M. R.; Greenwood, C.; Thomson, A. J. *Adv. Inorg. Chem.* **1991**, *36*, 201. (d) Johnson, M. K.; Robinson, A. E.; Thomson, A. J. In *Iron Sulfur Proteins*; Spiro, T. G., Ed.; John Wiley and Sons: New York, Chichester, Brisbane, Toronto, Singapore, 1982; pp 367−406. (e) Thomson, A. J. In *Perspectives in Modern Chemical Spectroscopy*; Andrews, D. L., Ed.; Springer: Berlin, Heidelberg, New York, London, Paris, Tokyo, Hong Kong; pp 243−259. (f) Sutherland, J. C. *Methods Enzymol.* **1995**, *246*, 110. (g) Johnson, M. K. In *Metal Clusters in Proteins*; Que, L., Jr., Ed.; ACS Symposium Series 372; American Chemical Society: Washington, DC, 1988; pp 326−342.

(2) Solomon, E. I.; Pavel, E. G.; Loeb, K. E.; Campochiaro, C. *Coord. Chem. Rev.* **1995**, *144*, 369.

(3) Solomon, E. I.; Hanson, M. A. In *Inorganic Electronic Spectroscopy*; Solomon, E. I., Lever, A. B. P., Eds.; Wiley & Sons: New York, in press.

(4) (a) Stephens, P. J. *J. Chem. Phys.* **1970**, *52* (7), 3489. (b) Stephens, P. J. *Adv. Chem. Phys.* **1975**, *35*, 197. (c) Stephens, P. J. *Annu. Rev. Phys. Chem.* **1974**, *25*, 201. (d) Buckingham, A. D.; Stephens, P. J. *Annu. Rev. Phys. Chem.* **1966**, *17*, 399. See also: (e) Schatz, P. N.; McCaffery, *Q. Rev.* **1969**, 552.

10.1021/ic981264d CCC: $18.00
Published on Web 03/19/1999

The theory of MCD spectroscopy has been pioneered by Stephens[4] and concisely summarized in an excellent monograph by Piepho and Schatz[5] that also discusses the method of moments developed by Henry et al.[6] and advanced by Stephens and co-workers.[7] The theory shows that in the domain where the MCD signal is a linear function of the applied magnetic field the signal for a sample of randomly oriented molecules takes the form[4,5]

$$\frac{\Delta\epsilon}{E} = \frac{\epsilon_{LCP} - \epsilon_{RCP}}{E} = \frac{1}{dc}\frac{A_{LCP} - A_{RCP}}{E} = \gamma\beta_B B\left[\left(-\frac{\partial f(E)}{\partial E}\right)\bar{A}_1 + \left(\bar{B}_0 + \frac{\bar{C}_0}{kT}\right)f(E)\right] \quad (1)$$

where γ is a collection of constants, β_B is the Bohr magneton, k is the Boltzmann constant, T is the absolute temperature, B is the magnetic flux density, $f(E)$ is a line shape function, d is the path length, c is the concentration of the molecular species considered, and $E = h\nu$ is the energy of the incident radiation. $\bar{A}_1$, $\bar{B}_0$, and $\bar{C}_0$ are characteristic numbers that depend on the electronic and geometric structure of the molecule under investigation and the transition under study. While nonzero $\bar{C}_0$ requires the molecule to be paramagnetic, $\bar{A}_1$ and $\bar{B}_0$ also exist for molecules in spin singlet ground states ($\bar{A}_1$ only if there is orbital degeneracy) and make MCD a universal phenomenon that occurs in all matter.[4,5] In practice it is commonly observed that for paramagnetic transition metal complexes studied near liquid helium temperatures the temperature dependent $\bar{C}_0$ term dominates the MCD spectrum, and this term is therefore the focus of this study.

Early on it was demonstrated that MCD *C*-term signs could be used to unambiguously assign the charge transfer (CT) spectrum of $[Fe(CN)_6]^{3-}$.[8] A number of similar applications were made,[9−15] and it was also realized that spin−orbit coupling (SOC) plays an important role for determining the *C*-term signs and magnitudes.[15] Summaries of the theoretical formalism necessary to treat high-symmetry cases are available.[5,16] Gerstman and Brill developed a model for the d−d transitions of low-symmetry mononuclear Cu(II) complexes based on a crystal field like model where d/p mixing accounts for the transition intensities. The importance of SOC was demonstrated[17] and a similar model was also applied in ref 18. To our knowledge the first direct molecular obital (MO) calculation of *C*-term signs was undertaken for the cupric active site of plastocyanin based on the Xα-SW electronic structure method,[19] and this led to fair agreement with the experimental spectrum, thus providing an experimentally calibrated bonding picture. Recently, a SCF-MO-CI model including SOC and based on the semiempirical INDO/S model was developed for the calculation of MCD *C*-terms and applied to biologically relevant copper complexes,[20] namely, the Cu_A center.[21]

At very low temperatures and high magnetic fields the MCD $\bar{C}_0$-term is no longer linear with respect to B/T and levels off to its saturation limit. The origin of this effect is that the *C*-term intensity that is caused by unequal Boltzmann populations of the ground state Zeeman components is saturated in the sense that only the lowest Zeeman sublevel is populated at high fields and low temperatures. For an isolated Kramers doublet with an isotropic *g*-value, Stephens[4b] has shown that the MCD signal varies with B/T as

$$\frac{\Delta\epsilon}{E} = A_{satlim}\tanh\left(\frac{g\beta_B B}{2kT}\right)f(E) \quad (2)$$

and thus one can determine the ground state *g*-value from a plot of the MCD intensity versus the dimensionless variable $\beta_B B/2kT$ at fixed wavelength. Schatz et al.[22] considered the more complicated case of axial *g*-matrices for molecules in the $D_{\infty h}$ point group and its subgroups and also showed how to correct for the presence of *B*-terms. Johnson and Thomson[23] extended the analysis to the case of rhombic *g*-matrices and also allowed for the presence of z-polarization. Application was made to hemoproteins. In the cases where $S > {}^1/_2$, more than two Zeeman components may be MCD active and the analysis is much more difficult. An approach applied by Stephens and co-workers showed that the zero-field splittings (ZFSs) of high-spin ferric hemoproteins could be determined in the linear region of the variable-temperature MCD experiment by analyzing the Boltzmann population of noninteracting or weakly interacting Kram-

(5) Piepho, S. B.; Schatz, P. N. *Group Theory in Spectroscopy with Applications to Magnetic Circular Dichroism*; John Wiley & Sons: New York, Chichester, Brisbane, Toronto, Singapore, 1983.
(6) Henry, C. H.; Schnatterly, S. E.; Slichter, C. P. *Phys. Rev.* **1965**, *137* (2A), A583.
(7) (a) Stephens, P. J. *Chem. Phys. Lett.* **1968**, *2* (4), 241. (b) Osborne, G. A.; Stephens, P. J. *J. Chem. Phys.* **1972**, *56* (1), 609.
(8) Stephens, P. J. *Inorg. Chem.* **1965**, *4* (12), 1690.
(9) (a) McCaffery, A. J.; Stephens, P. J.; Schatz, P. N. *Inorg. Chem.* **1967**, *6* (9), 1614. (b) Stephens, P. J.; Suetaak, W.; Schatz, P. N. *J. Chem. Phys.* **1966**, *44* (12), 4592. (c) Stephens, P. J. *J. Chem. Phys.* **1965**, *43* (12), 4444.
(10) (a) Schatz, P. N.; McCaffery, A. J.; Suetaka, W.; Henning, G. N.; Ritchie, A. B.; Stephens, P. J. *J. Chem. Phys.* **1966**, *45* (2), 722. (b) Piepho, S. B.; Lester, T. E.; McCaffery, A. J.; Dickinson, J. R.; Schatz, P. N. *Mol. Phys.* **1970**, *19* (6), 781.
(11) (a) Bird, B. D.; Briat, B.; Day, P.; Rivoal, J. C. *Symp. Faraday Soc.* **1969**, *3*, 70. (b) Rivoal, J. C.; Briat, B. *Mol. Phys.* **1974**, *27* (4), 1081. (c) Harding, M. J.; Briat, B. *Mol. Phys.* **1974**, *27* (5), 1153. (d) Petit, R. H.; Briat, B. *Mol. Phys.* **1974**, *27* (5), 1373. (e) Briat, B.; Canit, J. C. *Mol. Phys.* **1983**, *48* (1), 33.
(12) (a) Neuenschwander, K.; Güdel, H. U.; Collingwood, J. C.; Schatz, P. N. *Inorg. Chem.* **1983**, *22*, 1712. (b) Collingwood, J. C.; Schwartz, R. W.; Schatz, P. N. *Mol. Phys.* **1974**, *27* (5), 1291. (c) Ferguson, J.; Krausz, E. R.; Gugenheim, H. J. *Mol. Phys.* **1974**, *27* (3), 577. (e) Harding, M. J.; Billardon, M.; Kramer, A. *Mol. Phys.* **1974**, *27* (2), 457.
(13) (a) Deaton, J. C.; Gebhard, M. S.; Solomon, E. I. *Inorg. Chem.* **1989**, *28*, 877. (b) Gebhard, M. S.; Deaton, J. C.; Koch, S. A.; Millar, M.; Solomon, E. I. *J. Am. Chem. Soc.* **1990**, *112*, 2217. (c) Karpishin, T. B.; Gebhard, M. S.; Solomon, E. I.; Raymond, K. N. *J. Am. Chem. Soc.* **1991**, *113*, 2977. (d) Carducci, M. D.; Brown, C.; Solomon, E. I.; Enemark, J. H. *J. Am. Chem. Soc.* **1994**, *116*, 11856. (e) Ross, P. K.; Allendorf, M. D.; Solomon, E. I. *J. Am. Chem. Soc.* **1989**, *111*, 4009.
(14) (a) Kato, H.; Gohda, J. *Bull. Chem. Soc. Jpn.* **1973**, *46*, 636. (b) Kobayashi, H.; Korybut-Daskiewicz, B. *Bull. Chem. Soc. Jpn.* **1972**, *45*, 285. (c) Kato, H. *Mol. Phys.* **1972**, *24* (1), 81. (d) Harding, M. J.; Mason, S. F.; Robbins, D. J.; Thomson, A. J. *Chem. Phys. Lett.* **1970**, *7* (1), 70.
(15) (a) Denning, R. G.; Spencer, J. A. *Symp. Faraday Soc.* **1969**, *3*, 84. (b) Gale, R.; McCaffery, A. J. *J. Chem. Soc., Dalton Trans.* **1973**, 1344.
(16) (a) Briat, B. In Day, P., Ed.; *Electronic States of Inorganic Compounds*; D. Reidel Pub.: Dordrecht, Holland, 1975. (b) Dobosh, P. A. *Mol. Phys.* **1974**, *27* (3), 689.
(17) Gerstman, B. S.; Brill, A. S. *J. Chem. Phys.* **1985**, *82* (3), 1212.
(18) Landrum, G. A.; Ekberg, C. A.; Whittaker, J. W. *Biophys. J.* **1995**, *69*, 674.
(19) Gewirth, A. A.; Solomon, E. I. *J. Am. Chem. Soc.* **1988**, *110*, 3811.
(20) Neese, F. Dissertation, University of Konstanz, Germany, 1997.
(21) Farrar, J. A.; Neese, F.; Lappalainen, P.; Kroneck, P. M. H.; Saraste, M.; Zumft, W. G.; Thomson, A. J. *J. Am. Chem. Soc.* **1996**, *118*, 11501.
(22) Schatz, P. N.; Mowery, R. L.; Krausz, E. R. *Mol. Phys.* **1978**, *35* (6), 1537.
(23) Johnson, M. K.; Thomson, A. J. *Biochem. J.* **1980**, *191*, 411.
(24) (a) Browett, W. R.; Fucaloro, A. F.; Morgan, T. V.; Stephens, P. J. *J. Am. Chem. Soc.* **1983**, *105*, 1868. (b) Stephens, P. J.; Jensen, G. M.; Devlin, F. J.; Morgan, T. V.; Stout, C. D.; Martin, A. E.; Burgess, B. K. *Biochemistry* **1991**, *30*, 3200.

ers doublets.[24] Similar analyses were also used by other workers.[25] Cheesman and Thomson have modeled the high-spin case by considering a "quasi-atomic" $^{2S+1}S \rightarrow {}^{2S+1}P$ transition with the ground state splitting described by a spin-Hamiltonian (SH) and the excited state assumed to be split by SOC.[1b,26] A complicated case is that of high-spin Fe(II) where a low-symmetry split $^5T_{2g}$ term is lowest in energy and the non-Kramers nature of the ground state and near orbital degeneracy must be taken into account. An approach to this problem has been developed that treats the system as a collection of zero-field split non-Kramers doublets and singlets and takes into account *B*-term corrections and z-polarization.[2,27] Extensive application has been made to high-spin ferrous active sites in mononuclear[28] and binuclear[29] non-heme iron containing metalloenzymes, which has led to detailed insight into their structures and reaction mechanisms.

The model that is developed in this paper is in several respects more general than previous treatments and, in fact, contains a number of the above mentioned results as special cases. The equations derived here allow the MCD *C*-term contributions of all $2S + 1$ components of a spatially nondegenerate ground state to be related to each other in a rigorous way. This requires only a few vector coupling coefficients that will be shown to be directly related to the spin-expectation values of the ground state Zeeman components, the behavior of which is well-known in terms of the magnetic properties of the electronic ground state. This considerably reduces the number of parameters required in the analysis of experimental data and gives a well-defined physical meaning to the remaining parameters. Moreover, the theory is valid over the entire range of magnetic field strength and therefore allows the information content of the complete field/temperature space to be exploited. The model is valid for any molecular orientation and can be applied to calculate the orientation-averaged MCD spectrum. It is also valid for the case of ground state magnetic coupling tensors of arbitrary symmetry and relative orientation, a case that had not been previously treated. Since the equations are formulated in terms of nonrelativistic Born−Oppenheimer (BO) wave functions computed in a suitable molecule fixed coordinate system, explicit recipes for the calculation of *C*-term signs arise and are applied to MO-type wave functions in both the high- and low-spin cases.

The model described here was introduced in a study of the electronic structure of the high-spin ferric complex [Fe(EDTA)-(O_2)]$^{3-}$ and has for the first time led to a successful simulation of the MCD magnetization curves for a system with $S > {}^1/_2$ over the entire temperature (1.6−25 K) and field (0−7 T) ranges, thus permitting concise spectral assignments to be made.[30] Here we develop the formal aspects of the model and explore its predictions in detail.

2. Theory

2.1. Basis of MCD. The MCD spectrum is defined as the differential absorption of left and right circularly polarized (CP) light (measured as the difference in extinction coefficients $\Delta\epsilon = \epsilon_{LCP} - \epsilon_{RCP}$) in the presence of a magnetic field. Thus, the natural circular dichroism (CD) signal at zero field has to be subtracted from the MCD signal. Using a variety of standard approximations, most notably the Born−Oppenheimer and Franck−Condon approximations, and the Fermi golden rule and assuming a pure electric dipole mechanism for the transition, the MCD signal is given by[5]

$$\frac{\Delta\epsilon}{E} = K\sum_{a,j}(N_a - N_j)[|\langle a|m_{LCP}|j\rangle|^2 - |\langle a|m_{RCP}|j\rangle|^2]f(E) \quad (3)$$

where a labels an initial quantum state (Boltzmann population N_a) and j a final state (Boltzmann population N_j) of the system and m_{LCP} and m_{RCP} are the transition dipole moment operators for left and right circularly polarized light in a laboratory fixed reference coordinate system. We shall assume $N_j = 0$ since all transitions we are interested in are to excited states at least an order of magnitude higher in energy than kT ($\approx$200 cm^{-1} at room temperature). K is a constant that contains among other things a correction for the effective electric field seen by the absorbing molecule,[4,5] and $f(E)$ is the band shape function. A more subtle assumption usually invoked is the rigid shift model that assumes that $f(E)$ is independent of the external magnetic field. For the purpose of this study it is sufficient to consider a δ-function band shape and refer to E as the transition energy.

The procedure usually followed is to derive MCD dispersion expressions in the laboratory fixed frame and then average the resulting expression over molecular orientations for a collection of randomly oriented molecules. In this paper we follow a different route and first express the basic MCD equation in a molecule fixed coordinate system and then average over magnetic field orientations. This is advantageous for describing saturation behavior. In the laboratory fixed coordinate system the light beam travels along z, and the electric field components of the CP light are consequently in the x,y-directions. Using $m_{LCP,RCP} = m_x \mp im_y$ ($i = (-1)^{1/2}$) eq 3 becomes

$$\frac{\Delta\epsilon}{E} = 2iK\sum_{a,j}N_a(\langle a|m_x|j\rangle\langle j|m_y|a\rangle - \langle a|m_y|j\rangle\langle j|m_x|a\rangle) \quad (4)$$

It is now assumed that the electronic states in eq 4 have been computed in a suitable molecular coordinate system and the

(25) (a) Bennet, D. E.; Johnson, M. K. *Biochim. Biophys. Acta* **1987**, *911*, 71. (b) Johnson, M. K.; Bennet, D. E.; Fee, J. A.; Sweeny, W. V. *Biochim. Biophys. Acta* **1987**, *911*, 81. (c) Hamilton, C. L.; Scott, R. A.; Johnson, M. K. *J. Biol. Chem.* **1989**, *264*, (20), 11605. (d) Weth, M. T.; Tang, S. F.; Formicka, G.; Zeppezauer, M.; Johnson, M. K. *Inorg. Chem.* **1995**, *34*, 218. (e) Foote, N.; Gadsby, M. A.; Greenwood, C.; Thomson, A. J. *Biochem. J.* **1989**, *261*, 515. (f) Zhang, Y.; Gebhard, M. S.; Solomon, E. I. *J. Am. Chem. Soc.* **1991**, *113*, 5162.

(26) Cheesman, M. R. Dissertation, University of East Anglia, Norwich, U.K., 1988.

(27) (a) Whittaker, J. W.; Solomon, E. I. *J. Am. Chem. Soc.* **1988**, *110*, 5329. (b) Campochiaro, C.; Pavel, E. G.; Solomon, E. I. *Inorg. Chem.* **1995**, *34*, 4669. (c) Pavel, E. G.; Kitajima, N.; Solomon, E. I. *J. Am. Chem. Soc.* **1998**, *120*, 3949. (d) Pavel, E. G.; Solomon, E. I. In *Spectroscopic Methods in Bioinorganic Chemistry*; Solomon, E. I., Hodgson, K. O., Eds.; ACS Symposium Series 692; American Chemical Society: Washington, D.C., 1998.

(28) (a) Pavel, E. G.; Zhou, J.; Busby, R. W.; Gunsior, M.; Townsend, C. A.; Solomon, E. I. *J. Am. Chem. Soc.* **1998**, *120*, 743. (b) Loeb, K. E.; Zaleski, J. M.; Hess, C. D.; Hecht, S. M.; Solomon, E. I. *J. Am. Chem. Soc.* **1998**, *120*, 1249. (c) Loeb, K. E.; Westre, T. E.; Kappock, T. J.; Mitic, N.; Glasfeld, E.; Caradonna, J. P.; Hedman, B.; Hodgson, K. O.; Solomon, E. I. *J. Am. Chem. Soc.* **1997**, *119*, 1901. (d) Loeb, K. E.; Zaleski, J. M.; Westre, T. M.; Guajardo, R. J.; Mascharak, P. K.; Hedman, B.; Hodgson, K. O.; Solomon, E. I. *J. Am. Chem. Soc.* **1995**, *117*, 4545. (e) Pavlosky, M. A.; Zhang, Y.; Westre, T. E.; Gan, Q. F.; Pavel, E. G.; Campochiaro, C.; Hedman, B.; Hodgson, K. O.; Solomon, E. I. *J. Am. Chem. Soc.* **1995**, *117*, 4316.

(29) (a) Yang, Y. S.; McCormick, J. M.; Solomon, E. I. *J. Am. Chem. Soc.* **1997**, *119*, 11832. (b) Pulver, S.; Froland, W. A.; Fox, B. G.; Lipscomb, J. D.; Solomon, E. I. *J. Am. Chem. Soc.* **1993**, *115*, 12409. (c) Coates-Pulver, S.; Tong, W. H.; Bollinger, J. M.; Stubbe, J.; Solomon, E. I. *J. Am. Chem. Soc.* **1995**, *117*, 12664. (d) McCormick, J. M.; Reem, R. C.; Solomon, E. I. *J. Am. Chem. Soc.* **1990**, *113*, 9066. (e) Reem, R. C.; Solomon, E. I. *J. Am. Chem. Soc.* **1987**, *109*, 1216.

(30) Neese, F.; Solomon, E. I. *J. Am. Chem. Soc.* **1998**, *120*, 12829.

transition dipole moment vector is transformed to this frame using the matrix $\mathbf{A}(\theta,\phi,\eta)$ and $\vec{r}_{\mathrm{lab}} = \mathbf{A}\vec{r}_{\mathrm{mol}}$:[5,31]

$$\mathbf{A} = \begin{pmatrix} \cos\phi\cos\eta - \cos\theta\sin\phi\sin\eta & \sin\phi\cos\eta + \cos\theta\cos\phi\sin\eta & \sin\theta\sin\eta \\ -\cos\phi\sin\eta - \cos\theta\sin\phi\cos\eta & -\sin\phi\sin\eta + \cos\theta\cos\phi\cos\eta & \sin\theta\cos\eta \\ \sin\theta\sin\phi & -\sin\theta\cos\phi & \cos\phi \end{pmatrix} \tag{5}$$

Here θ is the angle of the light propagation direction with the molecular z-axis and ϕ is the angle that the projection of the propagation direction onto the molecular x,y-plane makes with the molecular y-axis. The third angle, η, is not relevant in the present application but included in eq 5 for completeness. From eq 4 and 5, eq 6 is obtained:

$$\frac{\Delta\epsilon}{E} = -\gamma\sum_{a,j} N_a\Big(\sum_{uvw} t_{uvw} l_u \,\mathrm{Im}\langle a|m_v|j\rangle\langle j|m_w|a\rangle\Big) \tag{6}$$

where $\gamma = 4K$, $t_{uvw} = 1$ for $uvw = xyz$, zxy, yzx and $t_{uvw} = 0$ otherwise, and l_u ($u = x,y,z$) is given by

$$\vec{l} = (\sin\theta\sin\phi, \sin\theta\cos\phi, \cos\theta) \tag{7}$$

In the next section we will assume explicit forms of the states a and j in the presence of SOC and examine the behavior of the system upon application of a magnetic field.

2.2. States and Transition Moments in the Presence of SOC. Any Born−Oppenheimer wave function can at least in principle be written as a product of a spatial function (that nevertheless depends on S via the antisymmetry requirement) and a spin function that depends on the total spin S and projection M of the state under consideration.[32] The key idea of the treatment is that, since the electric dipole matrix elements depend on the spatial part only (i.e., are independent of M), one only needs to relate the different M components of the ground and excited states by a straightforward vector coupling procedure. In this way the spin is dealt with directly and the remaining equations contain only the spatial parts of the states under consideration. This is graphically illustrated in Scheme 1.

Scheme 1

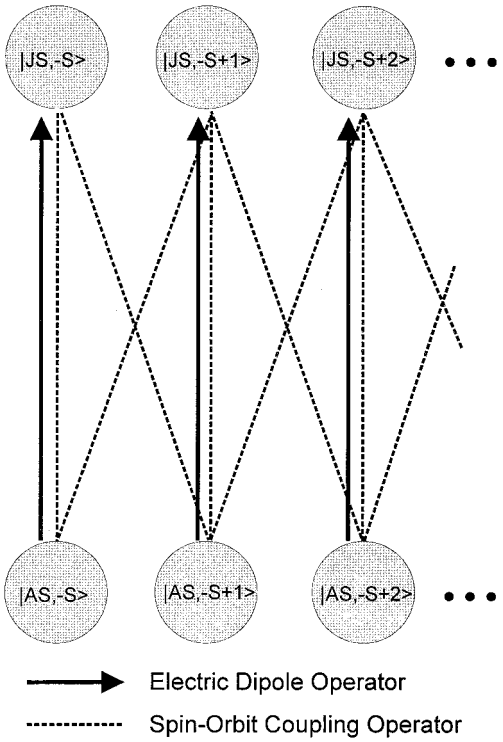

2.2.1. Zero-Order States. An orthonormal set of many electron wave functions $\{|\alpha S_\alpha M\rangle_0\}$ is assumed, where α is a compound label that contains all necessary quantum numbers except S_α and M is the total spin of state α and its projection onto the z-axis ($M = S_\alpha, S_\alpha - 1, ..., -S_\alpha$).[33] The set of states is assumed to diagonalize the BO Hamiltonian, i.e., $H_{\mathrm{BO}}|\alpha S_\alpha M\rangle_0 = E_\alpha|\alpha S_\alpha M\rangle_0$. The set of states is divided into four subsets, namely, (1) the A-set that contains $2S + 1$ components of the spatially nondegenerate ground state, (2) the J-set that is of the same spin as A and contains $2S + 1$ components of the spatially nondegenerate excited state J, (3) the K-set that contains all other states of spin S, and (4) the set of states with different S than the ground state that are neglected. Thus, we focus on spin-allowed transitions between spatially nondegenerate states. The restriction to spin-allowed transitions is not critical since spin-forbidden transitions do not have any intrinsic transition probability. High-symmetry cases involving spatial degeneracies are best handled by tensor operator methods.[5,16] The theory developed here applies to the case most commonly encountered in practice, for example in low-symmetry metalloprotein active sites.

2.2.2. Spin−Orbit Coupling. As a second step, SOC is accounted for by first-order nondegenerate pertubation theory. As in our recent work on ZFS,[34] the one-electron approximation to the SOC operator is used:[35]

$$H_{\mathrm{SOC}} \approx \sum_{N,i}\xi(r_{iN})\,\vec{l}_N(i)\,\vec{s}(i) = \sum_{m=0,\pm1}(-1)^m\sum_i h_{-m}(i)\,s_m(i) \tag{8}$$

with $\xi(r_{iN}) = (\alpha^2/2)(Z_N^{\mathrm{eff}}/r_{iN}^3)$. Here $\vec{l}_N(i)$ is the orbital angular momentum of the ith electron relative to nucleus N, $\vec{s}(i)$ is the spin-angular momentum operator for electron i, $h_{-m}(i)$ is a standard component of the reduced spin−orbit vector operator,[36] α is the fine structure constant ($\approx 1/137$), and Z_N^{eff} is the semiempirical effective charge of nucleus N.[37] Since $\vec{s}(i)$ is of type T[38] with respect to the total spin $\vec{S} = \sum_i\vec{s}(i)$, the Wigner−Eckhard theorem can be applied to calculate the SOC matrix elements between the BO states:[32,34]

(31) Schläfer, H. G.; Gliemann, G. *Einführung in die Ligandenfeldtheorie*; Akademische Verlagsgesellschaft Frankfurt am Main: Frankfurt, Germany, 1967; p 297.
(32) McWeeny, R. *Methods of Molecular Quantum Mechanics*; Academic Press: London, San Diego, New York, Boston, Sydney, Tokyo, Toronto, 1992.
(33) In what follows the subscript zero refers to the zero order (Born−Oppenheimer) states or matrix elements calculated between these states.
(34) Neese, F.; Solomon, E. I. *Inorg. Chem.* **1998**, *37*, 6568.
(35) (a) McClure, D. S. *J. Chem. Phys.* **1952**, *20*, 682. (b) McGlynn, S. P.; Vanquickenborne, L. G.; Kinoshita, M.; Carroll, D. G. *Introduction to Applied Quantum Chemistry*; Holt, Rinehart and Winston Inc.: New York, Chicago, San Francisco, Atlanta, Dallas, Montreal, Toronto, London, Sydney, 1972. (c) Misetich, A. A.; Buch, T. *J. Chem. Phys.* **1964**, *41* (8), 2524.
(36) McWeeny, R. *Spins in Chemistry*; Academic Press: New York, London, 1970.
(37) (a) Moores, W. H.; McWeeny, R. *Proc. R. Soc. London, A* **1973**, *332*, 365. (b) Abegg, P. W.; Ha, T. K. *Mol. Phys.* **1974**, *27* (3), 763. (c) Pasternak, R.; Wagniere, G. *J. Comput. Chem.* **1981**, *2* (3), 347. (d) Koseki, S.; Schmidt, M. W.; Gordon, M. S. *J. Chem. Phys.* **1992**, *96*, 10768. (e) Langhoff, S. R. *J. Chem. Phys.* **1974**, *61*, 1708. (f) Cohen, J. S.; Wadt, W. R.; Hay, P. J. *J. Chem. Phys.* **1979**, *71*, 2955.
(38) Griffith, J. S. *The Theory of Transition Metal Ions*; Cambridge University Press: Cambridge, 1964, p 34 ff.

$$\langle ASM|H_{SOC}|BSM'\rangle_0 = \sum_{m=0,\pm1} (-1)^m Y^{AB}_{-m} \begin{pmatrix} S & 1 & S \\ M' & m & M \end{pmatrix} \quad (9)$$

where

$$\begin{pmatrix} S & 1 & S \\ M' & m & M \end{pmatrix}$$

denotes a Clebsch−Gordon coefficient[39] (CGC) and the reduced matrix element Y^{AB}_{-m} is calculated from the standard components with $S = M$ as[34]

$$Y^{AB}_{-m} = \frac{\sqrt{S(S+1)}}{S} \langle ASS| \sum_i h_{-m}(i)\, s_0(i) |BSS\rangle_0 \quad (10)$$

Thus to first order in SOC the perturbed ground ($|ASM\rangle$) and excited ($|JSM\rangle$) states are

$$|ASM\rangle = |ASM\rangle_0 - \Delta^{-1}_{JA} \sum_{m=0,\pm1} (-1)^m Y^{JA}_{-m} \sum_{M'} \begin{pmatrix} S & 1 & S \\ M & m & M' \end{pmatrix} |JSM'\rangle_0 - \sum_{K\neq A,J} \Delta^{-1}_{KA} \sum_{m=0,\pm1} (-1)^m Y^{KA}_{-m} \sum_{M'} \begin{pmatrix} S & 1 & S \\ M & m & M' \end{pmatrix} |KSM'\rangle_0 \quad (11a)$$

$$|JSM\rangle = |JSM\rangle_0 + \Delta^{-1}_{JA} \sum_{m=0,\pm1} (-1)^m Y^{AJ}_{-m} \sum_{M'} \begin{pmatrix} S & 1 & S \\ M & m & M' \end{pmatrix} |ASM'\rangle_0 - \sum_{K\neq A,J} \Delta^{-1}_{KJ} \sum_{m=0,\pm1} (-1)^m Y^{KJ}_{-m} \sum_{M'} \begin{pmatrix} S & 1 & S \\ M & m & M' \end{pmatrix} |KSM'\rangle_0 \quad (11b)$$

where $\Delta_{IJ} = E_I - E_J$ and $\{|KSM'\rangle_0\}$ is the set of excited states of spin S excluding the set $|JSM\rangle_0$ ($M = -S...S$). Note from eq 9 that the selection rules contained in the CGCs require that $M - M' = 0, \pm1$ in order for a SOC matrix element to be nonzero.

2.2.3. Transition Dipole Moments. In order to calculate the transition moment between the perturbed states the electric dipole operator (in atomic units) is used:

$$\vec{m} = \sum_N Z_N \vec{R}_N - \sum_i \vec{r}_i \quad (12)$$

where Z_N is the charge of the Nth nucleus, $\vec{R}_N$ is its position vector, and $\vec{r}_i$ denotes the position of the ith electron. Since the operator in eq 12 is diagonal with respect to M for the BO states, the perturbed transition moment from eqs 11 and 12 is

$$\langle ASM|\vec{m}|JSM'\rangle = \delta_{MM'}\vec{D}^{AJ} + \Delta^{-1}_{JA} \sum_m (-1)^m Y^{AJ}_{-m} \begin{pmatrix} S & 1 & S \\ M' & m & M \end{pmatrix} (\vec{D}^{AA} - \vec{D}^{JJ}) - \sum_{K\neq A,J} \Delta^{-1}_{KJ} \sum_m (-1)^m Y^{KJ}_{-m} \begin{pmatrix} S & 1 & S \\ M' & m & M \end{pmatrix} \vec{D}^{AK} - \sum_{K\neq A,J} \Delta^{-1}_{KA} \sum_m (-1)^m Y^{AK}_{-m} \begin{pmatrix} S & 1 & S \\ M' & m & M \end{pmatrix} \vec{D}^{KJ} \quad (13)$$

where the abbreviations $\vec{D}^{AB} = \langle ASS|\vec{m}|BSS\rangle_0$ is used to denote the transition dipole moments involving the zero-order states and terms containing the product of energy denominators have been dropped. The first term in eq 13 is the unperturbed or intrinsic transition moment for the $A \rightarrow J$ transition, the second term comes from the SOC between states A and J and is proportional to the difference in dipole moments between the two states, the third term is interpreted as the borrowing of intensity from the transition $A \rightarrow K$ due to SOC between states K and J, and the final term is the intensity borrowed from the "virtual" excited state transition $J \rightarrow K$ induced by the SOC between states A and K. Such a first-order treatment of the SOC is approximate and cannot be expected to provide numerically accurate results for absolute C-term intensities. However, the perturbation approach gives insight into the general structure of the problem. Also, it would be straightforward to include excited states K in the treatment that have a total spin that is different from that of the ground state. Since these states do not carry intrinsic transition intensity, however, their effects only appear in higher order and would not change the results derived below.

2.3. MCD in the Presence of SOC. 2.3.1. Magnetic Field Perturbations. We consider the following effects of an applied magnetic field: (a) the field will induce a mixing between the M-components of the initial states $|ASM\rangle$ and of the final states $|JSM\rangle$; and (b) it will change the relative energies and therefore the populations N_a of the ground state sublevels. We will assume that the change in energy of the excited state components due to the field is small (neglect of A-terms) and that the initial state components only mix among themselves (neglect of out of state B-terms). We also neglect the excited state ZFS so that all components $|JSM\rangle$ ($M = -S...S$) are effectively degenerate.[40] Equation 6 is then summed over all $2S + 1$ components of the ground and excited state manifolds to obtain for the MCD of the transition $A \rightarrow J$:

$$\frac{\Delta\epsilon}{E} = -\gamma \sum_i N_i \Big(\sum_{uvw} t_{uvw} l_u \sum_{M,M'} \mathrm{Im}\, U^*_{Mi}\, U_{M'i} \sum_{M''} \times \langle ASM|m_v|JSM''\rangle \langle JSM''|m_w|ASM'\rangle \Big) \quad (14)$$

where **U** is a complex unitary matrix that describes the transformation from the states $|ASM\rangle$ to the magnetic field dependent states. The corresponding transformation for the J-set of states need not be carried out explicitly due to the principle of spectroscopic stability.[4,5,41] The index i sums over the $2S + 1$ components of the SOC and Zeeman perturbed ground state, and N_i is calculated from the usual Boltzmann statistics expression:

$$N_i = Z^{-1} \exp(-E^{(A)}_i/kT) \quad (15)$$

where $Z = \sum_i \exp(-E^{(A)}_i/kT)$ is the partition function and $E^{(A)}_i$ is the energy of the ith ground state sublevel. This treatment also assumes that there is no thermally accessible low-lying electronically excited state. In practice the coefficients **U** may be generated from the diagonalization of a suitably defined SH; for a mononuclear transition metal complex this SH would contain at least the Zeeman and ZFS terms. The idea of using a SH to describe the ground state sublevel splittings is similar to the Cheesman and Thomson approach,[1b,26] but the connection

(39) Rose, M. E. *Elementary Theory of Angular Momentum*; Dover Publications Inc.: New York, 1957.

(40) Thus, the average energy of the SOC and magnetic field split excited state components is taken as the excited state energy. In usual applications these splittings are 1−2 orders of magnitude smaller than the bandwidth of the optical transition studied.

(41) Due to the unitary nature of the transformation from the field independent to the field dependent states it is immaterial whether the summation over excited state components is performed over the original set or the transformed set.

to and treatment of the excited states is very different in the present model.

2.3.2. Explicit Connection of MCD and SOC. In the next step eq 13 is inserted into eq 14 to explicitly evaluate the effect of the SOC on the MCD response of the system. Attention is focused on the final term $\langle ASM|m_v|JSM''\rangle\langle JSM''|m_w|ASM'\rangle$. As each of the transition moment integrals in eq 13 contains four terms, there are 16 terms to be considered. Of these, the product of the first two terms (the intrinsic transition dipole moments) does not contribute to the MCD since it is entirely real and will be multiplied by the real number $|U_{Mi}|^2$. We also drop all terms that contain the products of energy denominators and concentrate on the leading terms that contain a single energy denominator. This leaves three contributions, $\Delta\epsilon^{(1,2,3)}/E$. These contributions are (a) terms that are proportional to the difference in dipole moments between the ground and the excited state that arise from direct SOC between states A and J, eqs 11a,b; (b) terms that arise from SOC of the excited state J with intermediate states K, eq 11b; and (c) terms that arise from SOC of intermediate states K with the ground state A, eq 11a. These three contributions will be treated in turn. However, on the basis of their similar structures, only one is presented in detail.

First, the relevant cross terms arising from the SOC between states A and J are obtained by inserting eq 13 into eq 14:

$$I^{(1)}_{MM'} = \sum_{M''}\left[\delta_{MM''}\vec{D}^{AJ}_{v} + \Delta^{-1}_{JA}\sum_{m}(-1)^{m}Y^{AJ}_{-m}\begin{pmatrix} S & 1 & S \\ M'' & m & M\end{pmatrix}\Delta\vec{D}^{AJ}_{v}\right]\left[\delta_{M'MM''}\vec{D}^{AJ}_{w} + \Delta^{-1}_{JA}\sum_{m}(-1)^{m}Y^{JA}_{-m}\begin{pmatrix} S & 1 & S \\ M' & m & M''\end{pmatrix}\Delta\vec{D}^{AJ}_{w}\right] \quad (16)$$

where $\Delta\vec{D}^{AJ} = \vec{D}^{AA} - \vec{D}^{JJ}$. Equation 16 is simplified using the CGCs tabulated by Rose,[39] the definition of vector operators[5,39] and eq 10 to give eq 17 (Supporting Information, section S1),

$$I^{(1)}_{MM'} = -(\vec{D}^{AJ}_{v}\,\Delta\vec{D}^{AJ}_{w} - \vec{D}^{AJ}_{w}\,\Delta\vec{D}^{AJ}_{v})\left\{\delta_{MM'}\frac{M}{S}\left(\frac{i\bar{L}^{AJ}_{z}}{\Delta_{JA}}\right) + \frac{1}{2}\delta_{MM'+1}\frac{\sqrt{(S+M)(S-M+1)}}{S}\left(\frac{i\bar{L}^{AJ}_{x} + \bar{L}^{AJ}_{y}}{\Delta_{JA}}\right) + \frac{1}{2}\delta_{MM'-1}\frac{\sqrt{(S-M)(S+M+1)}}{S}\left(\frac{i\bar{L}^{AJ}_{x} - \bar{L}^{AJ}_{y}}{\Delta_{JA}}\right)\right\} \quad (17)$$

where the shorthand notation was introduced:

$$\bar{L}^{AJ}_{p} = \mathrm{Im}\langle ASS|\sum_{i}h_{p}(i)\,s_{0}(i)|JSS\rangle_{0} \quad (18)$$

The quantities $\bar{L}^{AB}_{p}$ ($p = x, y, z$) are closely related to reduced matrix elements of the SOC operator. Note that $\langle ASS|\sum_i h_p(i)\,s_0(i)|JSS\rangle_0$ is purely imaginary if the BO eigenfunctions are real. Thus $\bar{L}^{AJ}_{p} = -\bar{L}^{JA}_{p}$. The benefit of having an explicit form is that now the real and imaginary parts of eq 14 can be identified. This is demonstrated for the diagonal terms ($M = M'$) that are given by

$$\frac{\Delta\epsilon^{(1)}_{\text{diagonalin}M}}{E} = -\gamma\sum_{i}N_{i}\Big(\sum_{uvw}t_{uvw}l_{u}\sum_{M}\mathrm{Im}|U_{Mi}|^{2}I^{(1)}_{MM}\Big) = \frac{\gamma}{S}\sum_{i}N_{i}\left(\sum_{uvw}t_{uvw}l_{u}(\vec{D}^{AJ}_{v}\,\Delta\vec{D}^{AJ}_{w} - \vec{D}^{AJ}_{w}\,\Delta\vec{D}^{AJ}_{v})\frac{\bar{L}^{AJ}_{z}}{\Delta_{JA}}\sum_{M}\left|U_{Mi}\right|^{2}M\right) = \frac{\gamma}{S}\vec{l}\,(\vec{D}^{AJ}\times\Delta\vec{D}^{AJ})\frac{\bar{L}^{AJ}_{z}}{\Delta_{JA}}\sum_{i}N_{i}\langle S_{z}\rangle_{i} \quad (19)$$

where the last line follows because the expectation value of the S_z operator for the ith ground state sublevel is given by

$$\langle S_{z}\rangle_{i} = \sum_{M}M|U_{Mi}|^{2} \quad (20)$$

Proceeding in the analogous way with the off-diagonal terms gives the combined result:

$$\frac{\Delta\epsilon^{(1)}}{E} = \frac{\gamma}{S}\vec{l}\,(\vec{D}^{AJ}\times\Delta\vec{D}^{JA})\Delta^{-1}_{JA}\sum_{i}N_{i}(\bar{L}^{AJ}_{x}\langle S_{x}\rangle_{i} + \bar{L}^{AJ}_{y}\langle S_{y}\rangle_{i} + \bar{L}^{AJ}_{z}\langle S_{z}\rangle_{i}) \quad (21)$$

The second set of terms corresponding to the contributions from the SOC mixing between the excited state J and intermediate states K are derived in an analogous way because the same CGCs are involved. The result for the MCD induced by SOC between states K and J (eq 11b) is

$$\frac{\Delta\epsilon^{(2)}}{E} = \frac{\gamma}{S}\sum_{K\neq A,J}\vec{l}\,(\vec{D}^{KA}\times\vec{D}^{AJ})\Delta^{-1}_{KJ}\sum_{i}N_{i}(\bar{L}^{KJ}_{x}\langle S_{x}\rangle_{i} + \bar{L}^{KJ}_{y}\langle S_{y}\rangle_{i} + \bar{L}^{KJ}_{z}\langle S_{z}\rangle_{i}) \quad (22)$$

Finally, the third contribution to the MCD induced by SOC between states A and K (eq 11a) is[42]

$$\frac{\Delta\epsilon^{(3)}}{E} = \frac{\gamma}{S}\sum_{K\neq A,J}\vec{l}\,(\vec{D}^{AJ}\times\vec{D}^{JK})\Delta^{-1}_{KA}\sum_{i}N_{i}(\bar{L}^{KA}_{x}\langle S_{x}\rangle_{i} + \bar{L}^{KA}_{y}\langle S_{y}\rangle_{i} + \bar{L}^{KA}_{z}\langle S_{z}\rangle_{i}) \quad (23)$$

Equations 21−23 predict the MCD sign and magnitude of a transition between spatially nondegenerate states A and J of a system as a function of magnetic field, temperature, and relative orientation. The temperature dependence is implicit in the values of the Boltzmann populations (N_i, eq 15), and the orientation dependence is explicit in $\vec{l}$, eq 7, and implicit in N_i and the spin-expectation values $\langle\vec{S}\rangle_i$. The orientation-averaged MCD spectrum is obtained by integrating eqs 21−23 over all magnetic field orientations:

$$\mathrm{MCD}_{\mathrm{av}}(E) = \frac{1}{4\pi}\int_{0}^{\pi}\int_{0}^{2\pi}\frac{\Delta\epsilon^{(1)} + \Delta\epsilon^{(2)} + \Delta\epsilon^{(3)}}{E}\sin\theta\,d\theta\,d\phi \quad (24)$$

Equations 21−23 show that some SOC must exist in the system in order for MCD to occur, which is consistent with our initial assumption that the states involved in the transition are spatially nondegenerate and is also in agreement with earlier results.[17,19] The SOC, of course, will be the more efficient the smaller the energy gap between the two states involved and the larger the SOC matrix elements. In addition there must be a transition moment component induced by the SOC that has a nonzero

(42) Each of the individual matrix elements for the electric dipole and reduced SOC components changes sign if a phase factor −1 is attached to one of the wave functions involved in eqs 21−23. However, each term contains a triple product of matrix elements in which each wave function appears twice. Thus, the overall expression is invariant to the choice of phases, as required.

projection on the magnetic field direction. Excited states with transition momements that are collinear with the one of interest ($A \rightarrow J$) will not contribute to MCD intensity.

Turning to the individual contributions, $\Delta\epsilon^{(1)}$ will usually be the smallest because the change of dipole moment will most likely occur in the direction in which charge is displaced during the transition and therefore be collinear with the transition dipole moment. Its contribution to the MCD intensity is therefore probably small, and we focus on the other two mechanisms.

2.3.3. Orthorhombic Systems. In orthorhombic point groups like D_{2h}, eqs 21−23 are particularly straightforward to interpret. For each pair of states there will only be one transition dipole moment component and one nonvanishing SOC component. If, for example, the transition $A \rightarrow J$ is x-polarized ($\vec{D}^{AJ} = (m_x^{AJ},0,0)^T$; $\Gamma_A \otimes \Gamma_J = B_{3u}$) and the transition $A \rightarrow K$ is y-polarized ($\vec{D}^{AK} = (0,m_y^{AK},0)^T$; $\Gamma_A \otimes \Gamma_K = B_{2u}$), then group theory shows that the only SOC component that can be nonzero is $\bar{L}_z^{KJ}$ ($\Gamma_J \otimes \Gamma_K = B_{1g} = \Gamma_{R_z}$) and eq 22 becomes

$$\frac{\Delta\epsilon}{E} = \frac{\gamma}{S} l_z M_{xy}^{\text{eff}} \sum_i N_i \langle S_z \rangle_i \tag{25}$$

where $M_{xy}^{\text{eff}} = m_x^{AJ}\, m_y^{AK}\, \bar{L}_z^{KJ}\, \Delta_{KJ}^{-1}$. A similar argument shows that if the transition $A \rightarrow K$ is z-polarized, it will give an MCD intensity to the transition $A \rightarrow J$ that is proportional to $l_y M_{xz}^{\text{eff}} \sum_i N_i \langle S_y \rangle_i$. If one has reason to assume that orthorhombic symmetry is an acceptable approximation, a reasonable expression to fit the MCD magnetization curves for randomly oriented samples is

$$\frac{\Delta\epsilon}{E} = \frac{\gamma}{4\pi S} \int_0^{\pi} \int_0^{2\pi} \sum_i N_i (l_x \langle S_x \rangle_i M_{yz}^{\text{eff}} + l_y \langle S_y \rangle_i M_{xz}^{\text{eff}} + l_z \langle S_z \rangle_i M_{xy}^{\text{eff}}) \sin\theta \, d\theta \, d\phi r \tag{26}$$

The convenience gained here is that one does not have to deal with the complexities of explicit SOC calculations if a comparative analysis of experimental data is required. Once one has obtained values for M_{xy}^{eff}, M_{xz}^{eff}, and M_{yz}^{eff}, these numbers can be subjected to theoretical analysis in much the same way as SH parameters are amenable to theoretical study.

2.3.4. Equations in Terms of Molecular Orbitals. In a number of cases it will be possible to approximate the states $|ASS\rangle$ by single determinantal wave functions. If a wave function for spin S can be represented by a single normalized Slater determinant (denoted as $|...|$) with n doubly and m singly occupied orbitals, it is of the high-spin type:

$$|ASS\rangle = |\psi_1 \bar{\psi}_1 ... \psi_n \bar{\psi}_n \psi_{o_1} ... \psi_{o_m}| \tag{27}$$

An excited state in which an electron is promoted from a doubly occupied into one of the singly occupied MOs is also an eigenfunction of S^2 and S_z with the same eigenvalue:

$$|I_i^{o_j} SS\rangle = |\psi_1 \bar{\psi}_1 ... \psi_i \bar{\psi}_{o_j} ... \psi_n \bar{\psi}_n \psi_{o_1} ... \psi_{o_m}| \tag{28}$$

Likewise, if an electron is promoted from one of the singly occupied orbitals to an empty orbital, a single determinant spin eigenfunction is obtained:

$$|II_{o_i}^a SS\rangle = |\psi_1 \bar{\psi}_1 ... \psi_n \bar{\psi}_n \psi_{o_1} ... \psi_a ... \psi_{o_m}| \tag{29}$$

The necessary matrix elements required to evaluate eqs 21−23 using eqs 27−29 are collected in Tables 1 and 2 and will be used in section 3.2.1 to derive C-term signs for $S = {}^1/_2$ systems and in 3.2.2 for $S = {}^5/_2$ systems. The case where an electron is promoted from a doubly occupied into an empty orbital is more complicated because it leads to several states of the same multiplicity as well as states of different multiplicities. The same is true for an electron promoted from one of the singly occupied orbitals into another singly occupied orbital with an accompanying spin flip. Several methods are available to construct spin eigenfunctions under these circumstances.[43] However, these situations are best handled on a case by case basis.

Table 1. Expressions for Reduced SOC integrals, $\bar{L}_p^{AB}$, Eq 18, in Terms of Molecular Orbitals Required for C-Term Calculations in Terms of the States in Eqs 27−29

	$\lvert ASS\rangle$	$\lvert I_j^{o_i} SS\rangle$	$\lvert II_{o_j}^b SS\rangle$
$\langle ASS\rvert$	0	$-{}^1/_2 \bar{L}_{1p}^{jo_j}$	${}^1/_2 \bar{L}_{1p}^{o_j b}$
$\langle I_i^{o_i} SS\rvert$	$-{}^1/_2 \bar{L}_{1p}^{o_i i}$	${}^1/_2 \delta_{o_i o_j}(1-\delta_{ij}) \bar{L}_{1p}^{ji}$ $-{}^1/_2 \delta_{ij}(1-\delta_{o_i o_j}) \bar{L}_{1p}^{o_i o_j}$	0
$\langle II_{o_i}^a SS\rvert$	${}^1/_2 \bar{L}_{1p}^{ao_i}$	0	${}^1/_2 \delta_{o_i o_j}(1-\delta_{ab}) \bar{L}_{1p}^{ab}$ $-{}^1/_2 \delta_{ab}(1-\delta_{o_i o_j}) \bar{L}_{1p}^{o_j o_i}$

[a] The following abbreviation is used: $\bar{L}_{1p}^{ij} \equiv \text{Im}\langle \psi_i | \sum_A \xi(r_A) l_{A,p} | \psi_j \rangle$.

Table 2. Expressions for Electric Dipole Matrix Elements, $\vec{D}^{AB}$, in Terms of Molecular Orbitals Required for C-Term Calculations in Terms of the States in Eqs 27−29[a]

	$\lvert ASS\rangle$	$\lvert I_j^{o_i} SS\rangle$	$\lvert II_{o_j}^b SS\rangle$
$\langle ASS\rvert$	$\vec{D}^{AA}$	$-\langle \psi_j \lvert \vec{r} \rvert \psi_{o_i} \rangle$	$-\langle \psi_{o_j} \lvert \vec{r} \rvert \psi_b \rangle$
$\langle I_i^{o_i} SS\rvert$	$-\langle \psi_{o_i} \lvert \vec{r} \rvert \psi_i \rangle$	$\delta_{ij}\delta_{o_i o_j} \vec{D}^{I^{o_i}I^{o_j}}$ $+\delta_{o_i o_j}(1-\delta_{ij}) \langle \psi_j \lvert \vec{r} \rvert \psi_i \rangle$ $-\delta_{ij}(1-\delta_{o_i o_j}) \langle \psi_{o_i} \lvert \vec{r} \rvert \psi_{o_j} \rangle$	0
$\langle II_{o_i}^a SS\rvert$	$-\langle \psi_a \lvert \vec{r} \rvert \psi_{o_i} \rangle$	0	$\delta_{ab}\delta_{o_i o_j} \vec{D}^{II^a{}_{o_i} II^a{}_{o_j}}$ $-\delta_{o_i o_j}(1-\delta_{ab}) \langle \psi_a \lvert \vec{r} \rvert \psi_b \rangle$ $+\delta_{ab}(1-\delta_{o_i o_j}) \langle \psi_{o_j} \lvert \vec{r} \rvert \psi_{o_i} \rangle$

[a] $\vec{D}^{JJ}$ is the dipole moment of state J.

3. Applications

In this section the methodology from section 2 is applied to two important cases. All calculations are based on eqs 21−23 and 26, and all expressions given in this section follow from these equations. In 3.1 the equations are used in their general form to analyze the saturation magnetization behavior for $S = {}^1/_2$ and $S = {}^5/_2$ systems. For both cases the information content of the experimental data is critically evaluated by systematic simulations. In section 3.2 the limit of weak magnetic fields is taken, permitting calculation of C-term signs from MO wave functions. Application is made again to $S = {}^1/_2$ and $S = {}^5/_2$. These choices of spin states are motivated by our interest in the ferric active sites of mononuclear non-heme iron enzymes that may have either high- or low-spin ground states[2,44] and frequently display rich MCD C-term spectra due to d−d ($S = {}^1/_2$) and LMCT transitions ($S = {}^1/_2$ and $S = {}^5/_2$). However, the conclusions that will be drawn have a wider range of applicability.

3.1. Saturation Magnetization. 3.1.1. Simulation Program. The simulations described in this section are based on the use of the standard SH:[45]

(43) Pauncz, R. *Spin Eigenfunctions. Construction and use*; Plenum Press: New York and London, 1979.
(44) (a) Que, L., Jr.; Ho, R. Y. N. *Chem. Rev.* **1996**, *96*, 2607. (b) Solomon, E. I.; Zhou, J.; Neese, F.; Pavel, E. G. *Chem. Biol.* **1997**, *11*, 795. (c) Burger, R. M. *Chem. Rev.* **1998**, *98*, 1153. (d) Ellison, J.; Nienstedt, A.; Shoner, S. C.; Barnhart, D.; Cowen, J. A.; Kovacs, J. A. *J. Am. Chem. Soc.* **1998**, *120*, 5691.
(45) Abragam, A.; Bleaney, B. *Electron Paramagnetic Resonance of Transition Ions*; Clarendon Press: Oxford, 1970.

$$\hat{H}_{\text{spin}} = \beta_B \vec{B}\mathbf{g}\vec{S} + D[S_z^2 - (1/3)S(S+1)] + E[S_x^2 - S_y^2] \quad (30)$$

where the reference coordinate system diagonalizes the *D*-tensor and leads to $0 \le E/D \le 1/3$.[46] For $S = {}^1/_2$ there is no ZFS and the principle coordinate system of the *g*-matrix is taken as the reference frame.

A two-dimensional numerical Gauss−Legendre integration of eq 26 is performed with a variable number of integration points.[47] Since the integrand is a fairly smooth function, a large number of points is not required. For each magnetic field point and orientation, the SH in eq 30 is diagonalized, and spin expectation values are calculated from the resulting eigenvectors as in eq 31 for the *i*th level:

$$\langle S_p \rangle_i = \sum_{M,M'} U^*_{Mi} U_{M'i} \langle SM|S_p|SM'\rangle \quad (31)$$

The Boltzmann populations, eq 15, are evaluated from the eigenvalues. Experimental data are analyzed by fitting the effective transition moment products M_{xy}^{eff}, M_{xz}^{eff}, M_{yz}^{eff}, eq 26, and/or the SH parameters together with a scaling parameter $A_{\text{satlim}} = \gamma/(4\pi S)$. The fits can be done with either a Simplex or a Levenberg−Marquadt algorithm.[47,48]

3.1.2. $S = {}^1/_2$ Systems. For the case of an $S = {}^1/_2$ system the SH eigenvalue problem is readily solved and gives the energies of the ground state Kramers doublet ($i = 1,2$):

$$E_{1,2}^{(A)} = \mp {}^1/_2 g\beta_B B \quad (32)$$

with $g = (G_x^2 + G_y^2 + G_z^2)^{1/2}$ and $G_p = l_p g_p$. The elements of the matrix **U** can also be worked out analytically:

$$\mathbf{U} = \frac{1}{\sqrt{2}} \begin{pmatrix} -qp & p \\ \text{p} & +q^* p \end{pmatrix} \qquad p = \sqrt{\frac{G_x^2 + G_y^2}{g(g - G_z)}}$$
$$q = \frac{g - G_z}{G_x + \text{i}G_y} \quad (33)$$

The expectation values for the ground state Kramers doublet are given by

$$\langle \vec{S} \rangle_{1,2} = \mp {}^1/_2 g^{-1}(G_x, G_y, G_z) \quad (34)$$

Thus eqs 22 and 23 become

$$\frac{\Delta\epsilon^{(2)}}{E} = -\frac{\gamma}{g} \tanh\left(\frac{g\beta_B B}{2kT}\right) \sum_{K \ne A,J} \vec{l}\,(\vec{D}^{KA} \times \vec{D}^{AJ}) \Delta_{KJ}^{-1} (l_x g_x \bar{L}_x^{KJ} + l_y g_y \bar{L}_y^{KJ} + l_z g_z \bar{L}_z^{KJ}) \quad (35a)$$

$$\frac{\Delta\epsilon^{(3)}}{E} = -\frac{\gamma}{g} \tanh\left(\frac{g\beta_B B}{2kT}\right) \sum_{K \ne A,J} \vec{l}\,(\vec{D}^{AJ} \times \vec{D}^{JK}) \Delta_{KA}^{-1} (l_x g_x \bar{L}_x^{KA} + l_y g_y \bar{L}_y^{KA} + l_z g_z \bar{L}_z^{KA}) \quad (35b)$$

The integral arising from orientational averaging of eq 35 cannot be evaluated in closed form. However, examination of the properties of the integrand under inversion reveals that the terms containing products $l_i l_j$ ($i \ne j$) yield zero and therefore eqs 35a and 35b can be combined into the form

$$\frac{\Delta\epsilon_{\text{av}}}{E} = -\frac{\gamma}{4\pi} \int_\theta \int_\phi \tanh\left(\frac{g\beta_B B}{2kT}\right) \frac{\sin\theta}{g} (l_x^2 g_x M_{yz}^{\text{eff}} + l_y^2 g_y M_{xz}^{\text{eff}} + l_z^2 g_z M_{xy}^{\text{eff}})\, \mathrm{d}\theta\, \mathrm{d}\phi \quad (36)$$

where from eqs 35a and 35b the effective transition moment products M_{ij}^{eff} can be identified as

$$M_{xy}^{\text{eff}} = \sum_{K \ne A,J} (\vec{D}_x^{KA} \vec{D}_y^{JK} - \vec{D}_y^{KA} \vec{D}_x^{AJ}) \frac{\bar{L}_z^{KJ}}{\Delta_{KJ}} + (\vec{D}_x^{AJ} \vec{D}_y^{JK} - \vec{D}_y^{AJ} \vec{D}_x^{JK}) \frac{\bar{L}_z^{KA}}{\Delta_{KA}} \quad (37)$$

and analogously for M_{xz}^{eff} and M_{yz}^{eff}. From eq 36 the well-known result follows that the ratio of the saturation limit to the initial slope of the magnetization curve equals $1/g$ in the case of an isotropic *g*-matrix and $1.5/g_{\|}$ for an axial *g*-matrix with $g_\perp = 0$ and an *x*,*y*-polarized transition.[1b,2,23]

Equation 36 is the generalization of other well-known equations from the literature that either assum axially symmetric *g*-matrices or assume that the *x*-polarized intensity is equal to the *y*-polarized intensity, or both.[1,23] It also quantifies the frequently quoted expression $\bar{C}_0 \propto g_x M_{yz} + g_y M_{xz} + g_z M_{xy}$.[1,17] Equation 36 is particularly suitable for the analysis of experimental data. The ground state *g*-values are usually known with high accuracy from EPR spectroscopy, which means that a fit of an experimental magnetization curve to eq 36 provides information about the effective transition dipole moments and therefore linear polarizations. If it is assumed that the sum in eq 37 is dominated by a single term, then $M_{xy}^{\text{eff}} = m_x m_y$, where m_x and m_y are the linear transition dipole moments determined from polarized absorption spectroscopy[49] (the intensity here is proportional to $|m_x|^2$ and $|m_y|^2$ with the electric vector of the light along *x* and *y*, respectively). In this case one can invert eq 37 to determine the % *x*-polarized intensity from

$$\%\, x = 100 \times \frac{(M_{xy}^{\text{eff}} M_{xz}^{\text{eff}})^2}{(M_{xy}^{\text{eff}} M_{xz}^{\text{eff}})^2 + (M_{xy}^{\text{eff}} M_{yz}^{\text{eff}})^2 + (M_{xz}^{\text{eff}} M_{yz}^{\text{eff}})^2} \quad (38)$$

and cyclic permutations of the indices gives the other polarizations. The conditions under which such an approach is feasible are illustrated in Figure 1. The sensitivity depends crucially on the anisotropy of the *g*-matrix because the initial slope of the magnetization curve is proportional to the *g*-value in the direction orthogonal to the plane of polarization (*vide infra*). In the case of an isotropic *g*-matrix there is of course no information on the transition polarization (Figure 1A). Anisotropies of $g_{\max} - g_{\min} \approx 0.25$ or smaller as is typical for many Cu(II) complexes lead to only small differences in the magnetization curves for differently polarized transitions (Figure 1B).

(46) Blumberg, W. E. In *Magnetic Resonance in Biological Systems*; Ehrenberg, A., Malmström, B., Eds.; Pergamon Press: Oxford, 1967; pp 110 ff.

(47) Press, W. H.; Teukolsky, S. A.; Vetterling, W. T.; Flannery, B. P. *Numerical Recipes in C*, 2nd ed.; Cambridge University Press: Cambridge, 1992.

(48) The derivative of the MCD magnetization with respect to the fit parameters required in the latter case is approximated by numerical central finite differences. Both methods are successful and require a similar amount of computer time since the smaller number of iterations needed for the Levenberg-Marquadt method is partly offset by the computationally demanding calculation of the numerical derivative. It is usually advantageous to manually explore as large a part of the parameter space as possible because experience indicates that the fits will frequently converge to local minima.

(49) The linear polarizations refer to the perturbed molecular states that have been corrected for SOC and not to the individual transition moments for the unperturbed states.

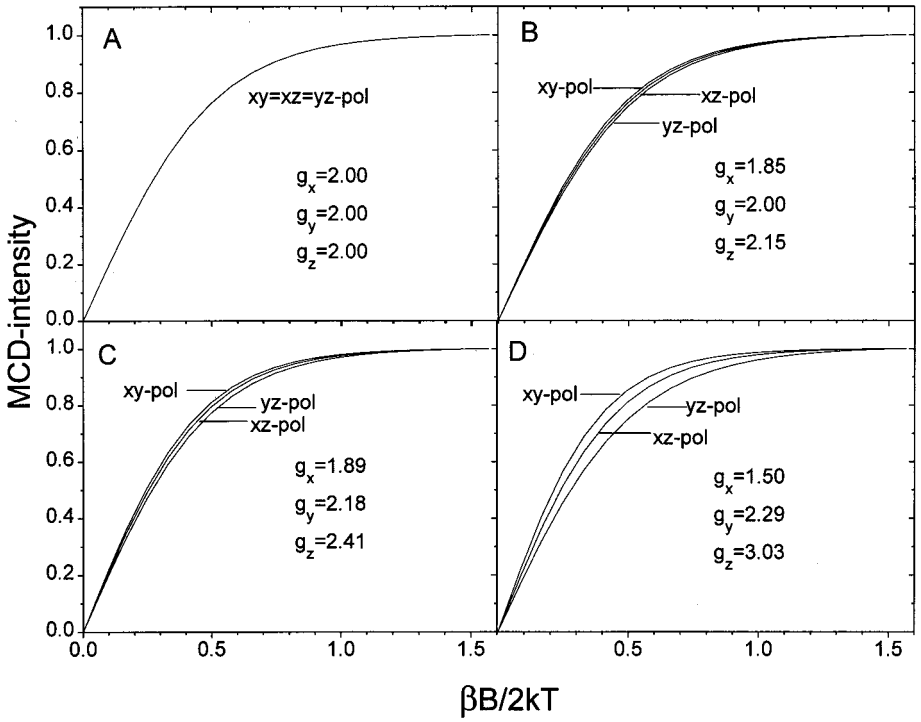

Figure 1. Predicted MCD saturation magnetization behavior for a $S = {}^1/_2$ system as a function of transition polarization and *g*-matrix anisotropy.

This means that very accurate experimental data would be required for a reliable determination of the transition polarizations. Panels C and D of Figure 1 show the situations with *g*-values typically observed for biologically relevant low-spin ferric sites.[44] Here the variation of magnetization behavior with transition polarization is recognizable and will allow the experimental determination of these polarizations from MCD studies.

3.1.3. High-Spin Systems. Application to $S = {}^5/_2$. In order to develop the MCD *C*-term saturation behavior we consider three limiting cases of the relative magnitudes of the ZFS and Zeeman terms and illustrated the performance of the theory by comparison to published experimental data. For convenience it is assumed here that the same coordinate system diagonalizes the *g*-matrix and the *D*-tensor and that the principal *g*-values are isotropic. These assumptions are usually satisfied by high-spin ferric complexes.

A. Large Zero-Field Splitting. In the case where the ZFS parameter *D* is much larger than the Zeeman splittings, Kramers systems with spin *S* approximately behave like a collection of $(2S + 1)/2$ independent "$S = {}^1/_2$" systems with effective *g*-values. Noting that, for the field applied along direction *p* for the *d*th doublet, one has $\langle S_p \rangle_d = \pm {}^1/_2(\tilde{g}_p^{(d)}/g_p)$, where the tilde denotes an effective *g*-value. Thus from eq 26 one expects that the effective *g*-values of the lowest populated levels that are perpendicular to the plane of polarization determine the behavior of the MCD saturation magnetization behavior. To facilitate the discussion, the effective *g*-values displayed by a $S = {}^5/_2$ system with large ZFS are collected in Table 3 for three different values of *E/D*.

A key result from section 2 of this paper (eqs 21−23, 26) is that the contributions of all Kramers doublets to the total MCD *C*-term intensity are related in a rigorous and simple way that follows from the vector coupling coefficients. In order to test the predictions of the theory, comparison is made to data reported in the literature. Browett et al.[24a] have used eq 39 to analyze the magnetization curves of high-spin ferric hemes in the linear region:

Table 3. Effective *g*-Values for a $S = {}^5/_2$ System with Large ZFS

		$\tilde{g}_x$	$\tilde{g}_y$	$\tilde{g}_z$
$E/D = 0$	$M_S = \pm {}^1/_2$	6.00	6.00	2.00
	$M_S = \pm {}^3/_2$	0.00	0.00	6.00
	$M_S = \pm {}^5/_2$	0.00	0.00	10.00
$E/D = 0.16$	"$M_S = \pm {}^1/_2$"	5.61	6.38	1.99
	"$M_S = \pm {}^3/_2$"	0.39	0.38	6.00
	"$M_S = \pm {}^5/_2$"	0.00	0.00	10.00
$E/D = {}^1/_3$	"$M_S = \pm {}^1/_2$"	0.86	9.69	0.61
	"$M_S = \pm {}^3/_2$"	4.29	4.29	4.29
	"$M_S = \pm {}^5/_2$"	0.86	0.61	9.69

$$\frac{\Delta\epsilon}{E} = \left(\sum_{d=1}^{3} \alpha_d \frac{c_d}{kT} + x\right) B \tag{39}$$

Here α_d is the fractional population of the *d*th Kramers doublet at zero magnetic field and the term *xB* was included to model *A*- and *B*-terms. The parameters $c_1 - c_3$ and the ZFS parameter *D* were then fitted to MCD data taken at constant field and variable temperatures. A value of $D \approx 6.9$ cm^{-1} was derived from Fe(TPP)Cl, a five-coordinated high-spin ferric heme.[24a] In order to predict the values of $c_1 - c_3$, it is important to note that the transitions studied are strongly *x,y* polarized.[50] In section 3.2.2 the general form of these coefficients will be derived. For the case studied by Browett et al. the *c*'s are given by

$$c_d = -{}^1/_{30}\gamma\beta_B M_{xy}^{\text{eff}}\, \tilde{g}_z^{(d)} \tag{40}$$

Equation 40 predicts that the *c*'s should have the following proportion: $\tilde{g}_z^{(1)}:\tilde{g}_z^{(2)}:\tilde{g}_z^{(3)} = 2{:}6{:}10$ (Table 3). The ratio reported for the 410 nm band of Fe(TPP)Cl is 1.52:5.32:10.41.[24a] The agreement is less good for the band at 432 nm (1.58:6.10:27.5) because c_3 is ≈2.7 times larger than expected. However, the theory still correctly predicts the trends observed experimentally.

(50) (a) Eaton, W. A.; Hochstrasser, R. M. *J. Chem. Phys.* **1967**, *46*, 2533. (b) Eaton, W. A.; Hochstrasser, R. M. *J. Chem. Phys.* **1968**, *49*, 985.

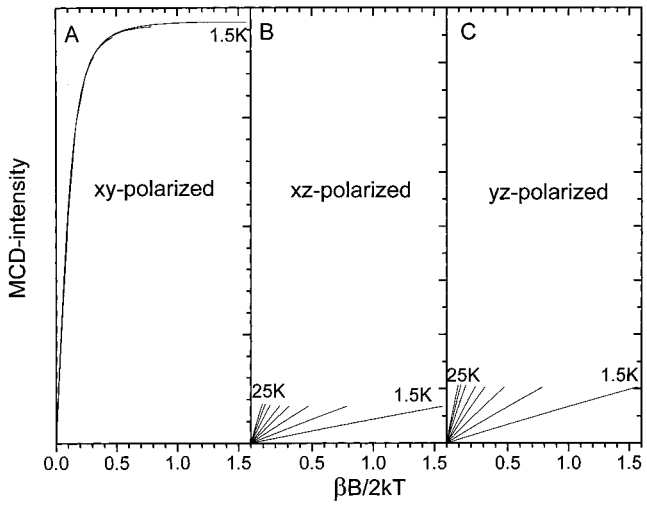

Figure 2. Predicted MCD saturation magnetization behavior for a $S = {}^5/_2$ system with large negative zero field splitting ($D = -10$ cm^{-1}, $E/D = 0$) as a function of transition polarization. Isotherms were calculated at 1.5, 3, 5, 7.5, 10, 15, 20, and 25 K for 20 field values between 0 and 7 T.

Note that this result also unambiguously establishes that D is positive for Fe(TPP)Cl, as would be expected for a five-coordinate high-spin ferric complex with approximate C_{4v} symmetry.[34] In order to explore the whole B/T space, numerical simulations as described in section 3.1.1 were performed for a range of D and E/D values and polarizations. A complete tabulation of the results is provided as Supporting Information (section S2). Figure 2 shows the behavior of a system with large negative ZFS ($D = -10$ cm^{-1}) and serves as an illustration for the general result (see S2) that, with increasing effective g-value perpendicular to the plane of polarization, (a) the initial slope of the magnetization curve increase, (b) the saturation limit increases, and (c) the nesting behavior (non-superposition) of the isotherms becomes less pronounced. Thus, for negative D and $E/D = 0$ the ground state Kramers doublet has a large value $\tilde{g}_z^{(1)} = 10$ (Table 3) leading to very steep, unnested behavior for x,y-polarized transitions. Alternatively from panels B and C of Figure 2 very small values $\tilde{g}_{x,y}^{(1)} = 0$ (Table 3), lead to extensive nesting and weak MCD. As can be seen from Table 3 the effective g-values for the ground state doublet of a $-D$ Kramers system are fairly insensitive to the value of E/D and thus there is almost no change of the MCD saturation magnetization with E/D (see Supporting Information, section S2).

By contrast, if D is positive and $E/D = 0$, the ground state Kramers doublet has a relatively small effective g-value $\tilde{g}_z^{(1)} = 2$ and larger values $\tilde{g}_{x,y}^{(1)} = 6$, and these are reflected in the saturation magnetization curves shown in Figure 3a. As seen in Table 3, $\tilde{g}_z^{(1)}$ is again a weak function of E/D and thus x,y-polarized transitions are insensitive to this value. However, $\tilde{g}_{x,y}^{(1)}$ are sensitive to E/D. In the rhombic limit ($E/D = {}^1/_3$), $\tilde{g}_y^{(1)}$ reaches a limiting value of 9.69, which leads to steep unnested MCD magnetization behavior of x,z-polarized transitions (Figure 3b,ii) whereas $\tilde{g}_x^{(1)}$ decreases to 0.61 and leads to similarly weak, nested behavior for x,y- and y,z-polarized transitions (figure 3b,i,iii).

In the analysis of MCD magnetization curves of systems with large ZFS, ambiguities always arise when effective g-values become comparable. For example it will be difficult to distinguish between a system with $D < 0$, $E/D = 0$, and x,y-polarization and a system with $D > 0$, $E/D = {}^1/_3$, and

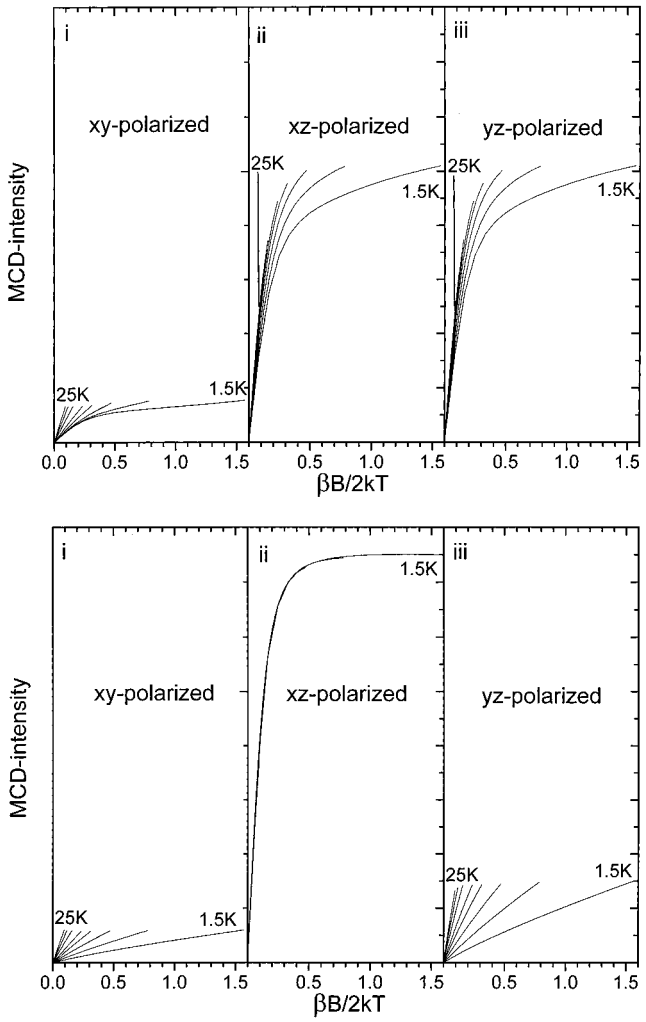

Figure 3. Predicted MCD saturation magnetization behavior for a $S = {}^5/_2$ system with large positive zero field splitting ($D = +10$ cm^{-1}) as a function of transition polarization and anisotropy. Isotherms were calculated at 1.5, 3, 5, 7.5, 10, 15, 20, and 25 K for 20 field values between 0 and 7 T: (a) $E/D = 0$; (b) $E/D = {}^1/_3$.

x,z-polarization. In these cases it would be important to have other experimental information available, especially the EPR spectrum or independent polarization information from single-crystal electronic spectroscopy. An additional point concerns the sign of D in the rhombic limit. As seen from Table 3, $\tilde{g}_{x,y,z}^{(1)}$ and $\tilde{g}_{x,y,z}^{(3)}$ are pairwise identical but their order is exchanged. For EPR and magnetic susceptibility measurements this means that $D > 0$ and $D < 0$ will lead to identical experimental results. The same is not necessarily true for MCD spectroscopy, where transitions of given polarization will lead to different magnetization behavior for $D > 0$ versus $D < 0$ due to the selection rules of the technique. However, in the case where the transition polarizations are not known, this distinguishability will not produce new insight.

B. Small Zero-Field Splitting. The opposite limit is obtained when ZFS is small compared to the Zeeman splitting. If the g-matrix is isotropic, the SH eigenvalue problem is again readily solved and yields pairs of states with quantum numbers $\pm M$ ($M = -S\cdots S$) quantized along the external field. The average over orientations implied by eq 26 can then be performed exactly. As is well-known in molecular magnetism[51] and pointed

(51) Kittel, C. *Introduction to Solid State Physics*, 6th ed.; Wiley & Sons: New York, 1986, pp 400−402.

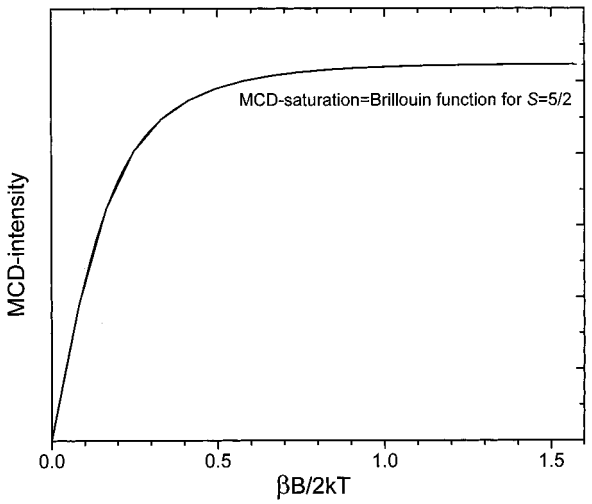

Figure 4. Predicted MCD saturation magnetization behavior for a $S = {}^5/_2$ system with no zero field splitting ($D = 0$). Isotherms were calculated at 1.5, 3, 5, 7.5, 10, 15, 20, and 25 K for 20 field values between 0 and 7 T. The Brillouin function for $S = {}^5/_2$ is superimposed.

out in the context of MCD by Graham,[52] the summation over the $2S + 1$ ground state components simply yields the Brillouin function B_S, for spin S:

$$\frac{\Delta\epsilon}{E} = K' B_S\left(\frac{g\beta B}{2kT}\right) = K'\left\{\frac{2S+1}{2S}\coth\left(\frac{(2S+1)g\beta_B B}{kT}\right) - \frac{1}{2S}\coth\left(\frac{g\beta_B B}{kT}\right)\right\} \quad (41)$$

where K' absorbs all constant factors. An example is shown in Figure 4 for $S = {}^5/_2$. Thus, in the limit of no ZFS there is no nesting in the saturation magnetization curves and MCD yields no information on transition polarizations.

It is important to recognize the limits of applicability of eq 41 because it is frequently used in the literature to infer the ground state spin S from MCD and magnetic measurements. As shown above, the absence of nesting does *not* imply small ZFS since it also occurs for large ZFS with a large effective g-value for the lowest doublet. In this case the spin state predicted by eq 41 can be seriously in error. Figure 5 shows the 1.5 K trace of the saturation magnetization curve for $S = {}^5/_2$, $D = -10$ cm^{-1}, $E/D = 0$ and x,y-polarization, i.e., an effective g-value of 10, together with the Brillouin functions for $S = {}^1/_2$ to $S = {}^9/_2$. As can be seen from Figure 5 the trace is closely reproduced by $B_{9/2}$, i.e., one would predict an S of ${}^9/_2$, where in reality $S = {}^5/_2$. Thus, unless there is independent experimental evidence for very small ZFS, eq 41 cannot be used with any degree of confidence to assign the ground state spin of a species with unknown ground state multiplicity.

If, however, the system is known to have a large ZFS and no nesting is observed in the MCD saturation magnetization, a possible approach is to determine the effective g-value of the transition by fitting the isotherms to a form $\Delta\epsilon/E = A_{\text{satlim}} \tanh(g_{\text{eff}}\beta_B B/2kT)$ appropriate for an effective "$S = {}^1/_2$" system and then infer the ground state spin from the knowledge of the effective g-values for a spin S system.[53]

C. Intermediate Zero-Field Splitting. The most complicated case is when the ZFS is on the order of a few wavenumbers. In this case the electron spin is initially quantized along the molecular z-direction by the ZFS. With increasing external field, the ZFS and Zeeman interactions become comparable and finally the field will be strong enough to completely align the electron spin along the external field direction. The behavior of the spin expectation values in this case depends on all contributing parameters and cannot be derived in closed form.[54] Thus, one relies on numerical simulations to analyze the experimental data over the entire B/T-parameter space. A feature common to all systems that are in the intermediate ZFS regime is the presence of substantial nesting behavior of the saturation magnetization curves. However, the observation of nesting does not require that the system is in the intermediate ZFS regime because extensive nesting is also possible for large ZFS (section 3.1.3.B). Here a combination of experimental techniques is necessary; for example, the temperature and microwave power dependence of the EPR spectrum can distinguish between the intermediate and strong ZFS limits.[55]

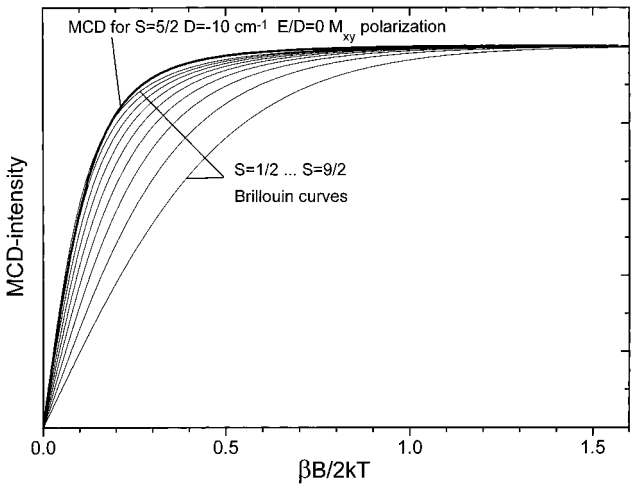

Figure 5. Comparison of the predicted MCD saturation magnetization behavior for a $S = {}^5/_2$ system with large negative zero field splitting (1.5 K trace, M_{xy} polarization from Figure 2) and the Brillouin functions for $S = {}^1/_2$ to $S = {}^9/_2$ (steps of 1).

Rather than presenting an exhaustive list of possible behaviors, two specific examples are analyzed that provide insight into the general behavior. Figure 6 shows representative results for systems with intermediate ZFS ($D = \mp 1$ cm^{-1}, $E/D = 0$, x,y-polarized transition). Focusing first on the 1.5 K trace of the $-D$ system in Figure 6A, it is observed that saturation magnetization first steeply increases, then reaches a maximum, and finally decreases. This effect is due to a change in quantization axis and is analyzed in more detail in Figure 7 and 8. Scheme 2 presents the splitting of the six ground state sublevels at zero magnetic field, leaving the $M_S = \mp {}^5/_2$ doublet lowest in energy for $D < 0$.

The splitting of these levels in an applied magnetic field is shown in Figure 7B for the field along the molecular z-axis ($\theta = 0$) and at an intermediate orientation ($\theta = \pi/4$) in Figure

(52) Graham, R. G. *Chem. Phys. Lett.* **1987**, *133* (3), 193.

(53) Note that there are also potential ambiguities in this approach due to the dependence of the effective g-values on E/D and of the isotherms on the transition polarization.

(54) As long as the applied magnetic field is very weak it is still possible to use the methods described in section 3.1.3.A, but this places emphasis on the region of the magnetization curve where the experimental data is necessarily the most noisy.

(55) (a) Yim, M. B.; Kuo, L. C.; Makinen, M. W. *J. Magn. Reson.* **1982**, *46*, 247. (b) Makinen, M. W.; Kuo, L. C.; Yim, M. B.; Wells, G. B.; Fukuyama, J. M.; Kim, J. E. *J. Am. Chem. Soc.* **1985**, *107*, 5245. (c) Aasa, R. *J. Chem. Phys.* **1970**, *52* (8), 3919. (d) Slappendel, S.; Veldink, G. A.; Vliegenthart, J. F. G.; Aasa, R.; Malmström, B. G. *Biochem. Biophys. Acta* **1980**, *642*, 30. (e) Pilbrow, J. R. *Transition Ion Electron Paramagnetic Resonance*; Oxford Science Publications, Clarendon Press: Oxford, 1990; Chapters 1 and 12.

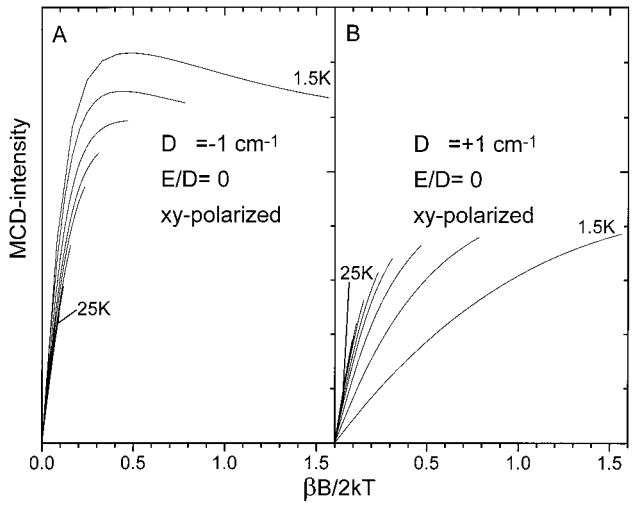

Figure 6. Predicted MCD saturation magnetization behavior for a $S = {}^5/_2$ system with intermediate zero field splitting ($|D| = 1$ cm^{-1}). Isotherms were calculated at 1.5, 3, 5, 7.5, 10, 15, 20, and 25 K for 20 field values between 0 and 7 T and $E/D = 0$: (A) $D = -1$ cm^{-1}; (B) $D = +1$ cm^{-1}.

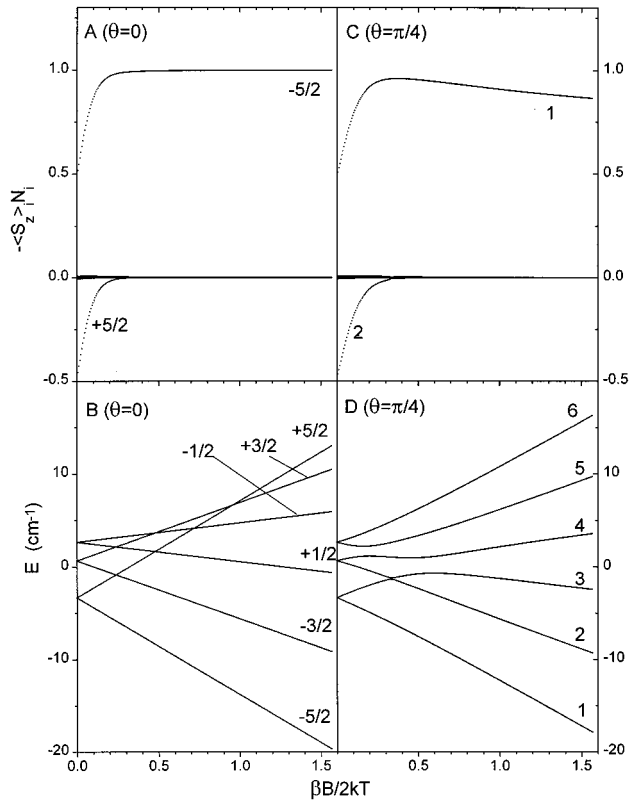

Figure 7. Behavior of a $S = {}^5/_2$ system with intermediate negative ZFS ($D = -1$ cm^{-1}, $E/D = 0$, $T = 1.5$ K, x,y-polarized transition). (A) Sum of the contributions of all ground state sublevels as a function of $\beta B/2kT$ at $\theta = 0$. (B) Energies of the ground state sublevels as a function of $\beta B/2kT$ at $\theta = 0$. (C) Sum of the contributions of all ground state sublevels as a function of $\beta B/2kT$ at $\theta = \pi/4$. (D) Energies of the ground state sublevels as a function of $\beta B/2kT$ at $\theta = \pi/4$.

7D. In Figure 7A the behavior of the contribution of all ground state sublevels to the total MCD intensity ($\propto \sum_i N_i \langle S_z \rangle_i$, eq 26) for $T = 1.5$ K is shown. It is observed that the lowest sublevel ($M_S = -{}^5/_2$) dominates the entire range of $\beta B/2kT$ and becomes the only contribution around $\beta B/2kT \approx 0.35$. However, the decrease of the integrated intensity in the MCD at $\beta B/2kT >$ 0.35 (1.5 K trace in Figure 6A) is not present in Figure 7A.

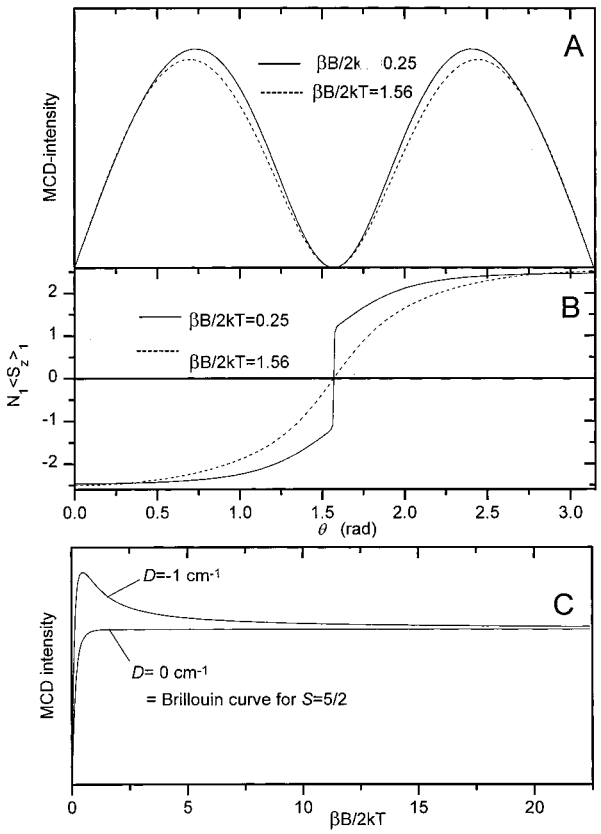

Figure 8. Contributions to the MCD saturation magnetization behavior of a $S = {}^5/_2$ system with intermediate negative ZFS ($D = -1$ cm^{-1}, $E/D = 0$, $T = 1.5$ K, x,y-polarized transition). (A) Sum of the contributions of all ground state sublevels as a function of magnetic field orientation for $\beta B/2kT = 0.25$ (—) and $\beta B/2kT = 1.56$ (---). The behavior is dominated by the lowest level (not shown). (B) Behavior of the spin expectation value $\langle S_z \rangle$ of the lowest sublevel weighted by its Boltzmann occupation as a function of magnetic field orientation for $\beta B/2kT = 0.25$ (—) and $\beta B/2kT = 1.56$ (---). (C) Magnetic field behavior to high fields ($B = 0-100$ T) of the MCD saturation magnetization curve for the above system compared to the Brillouin curve for $S = {}^5/_2$.

Scheme 2

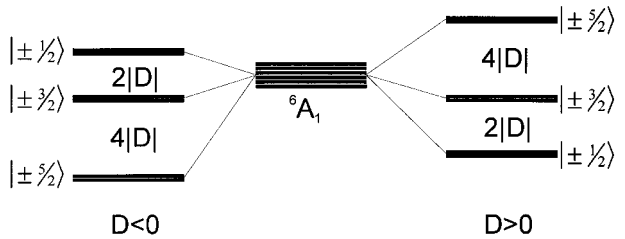

The origin of this decrease is analyzed in Figure 8. Figure 8A plots the net contribution to the total MCD intensity as a function of magnetic field orientation ($\theta = 0...\pi$) for the values $\beta B/2kT = 0.25$ (close to the maximum of the 1.5 K trace in Figure 6A) and $\beta B/2kT = 1.56$ (corresponding to the final point of this curve). As expected, the intensity vanishes at $\theta = 0$ due to the sin θ factor in the integrand which is related to the number of molecules that has the molecular z-axis aligned at an angle θ relative to the applied field. At $\theta = \pi/2$ the field is in the molecular x,y-plane and the total MCD intensity vanishes because there is no magnetization perpendicular to the plane of polarization (as required by eq 26). Therefore the integrand peaks at an intermediate angle $\theta = \pi/4$, and consequently the total MCD intensity in Figure 6A is dominated by the behavior

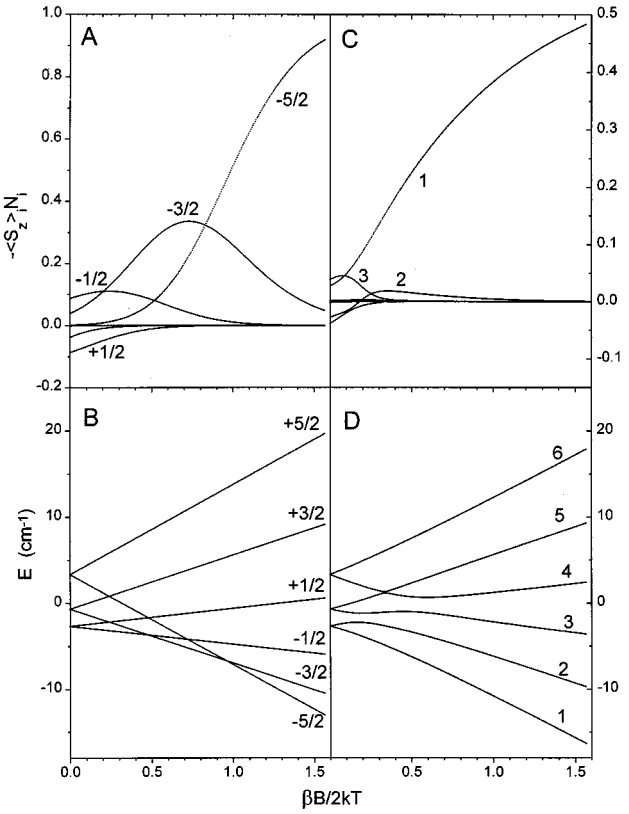

Figure 9. Behavior of a $S = {}^5/_2$ system with intermediate positive ZFS ($D = +1$ cm^{-1}, $E/D = 0$, $T = 1.5$ K, x,y-polarized transition). (A) Contributions of all ground state sublevels as a function of $\beta B/2kT$ at $\theta = 0$. (B) Energies of the ground state sublevels as a function of $\beta B/2kT$ at $\theta = 0$. (C) Contributions of all ground state sublevels as a function of $\beta B/2kT$ at $\theta = \pi/4$. (D) Energies of the ground state sublevels as a function of $\beta B/2kT$ at $\theta = \pi/4$.

at intermediate angles. From Figure 8A it is seen that for angles around $\theta = \pi/4$ and $\theta = 3\pi/4$ the intensity of the $\beta B/2kT = 1.56$ trace is systematically lower than that of the $\beta B/2kT = 0.25$ trace, thus accounting for the biphasic behavior of the 1.5 K trace in Figure 6A. As shown in Figure 8B, the origin of this effect can be traced back to the behavior of the spin-expectation value, $\langle S_z \rangle_1$, for the lowest energy sublevel. At small applied magnetic fields ($\beta B/2kT = 0.25$) the electron spin is dominantly quantized along the molecular z-axis by the ZFS. Therefore there is a rather rapid change of $\langle S_z \rangle_1$ when the field switches at $\theta = \pi/2$ from being along the molecular $+z$-direction to being along the molecular $-z$-direction. By contrast, at high applied magnetic fields ($\beta B/2kT = 1.56$), the electron spin is dominantly quantized along the field direction and therefore the projection onto the molecular z-axis is systematically smaller in magnitude than at low applied fields. Therefore, the total integrated MCD intensity is higher for $\beta B/2kT = 0.25$ relative to $\beta B/2kT = 1.56$ due to the behavior at intermediate angles. This is reflected in Figure 7C, which shows that for intermediate angles ($\theta = \pi/4$) the contribution of the lowest ground state sublevel parallels the behavior of the integrated intensity in Figure 7A. Note that is is not possible for a MCD band to change sign by this mechanism. Figure 8C shows that for extremely large fields the MCD intensity reaches a limiting value that is determined by the Brillouin function. This is expected from the results of section 3.1.3.B.

The analogous situation for a $+D$ system is analyzed in Figure 9. Figure 9B shows the variation of the ground state sublevel energies as a function of magnetic field. For small applied fields

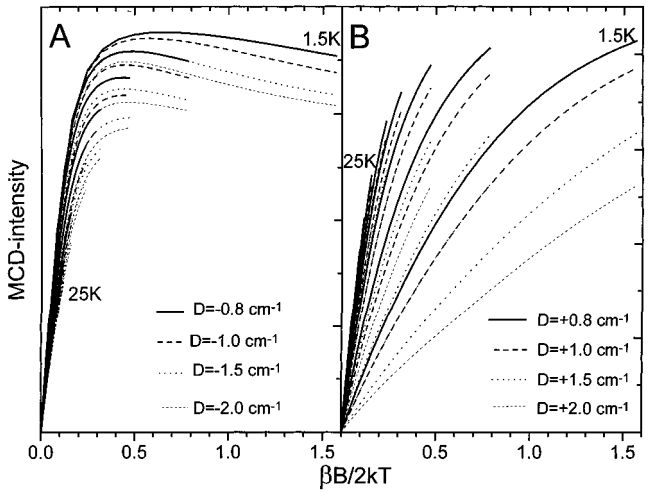

Figure 10. The predicted MCD saturation magnetization behavior of a $S = {}^5/_2$ system in the intermediate ZFS regime as a function of $|D|$ ($E/D = 0$): (A) negative D; (B) positive D.

the lowest level is $M_S = -{}^1/_2$, between $\beta B/2kT \approx 0.5$ and 1 ($T = 1.5$ K) it is $M_S = -{}^3/_2$, and for higher fields it is $M_S = -{}^5/_2$. Consequently many levels have contributions to the total MCD intensity as shown in Figure 9A. However, as seen in the previous case (Figure 8A), the integrated MCD intensity is dominated by the behavior at intermediate angles that is analyzed in Figure 9C,D for $\theta = \pi/4$. Again the behavior of the lowest sublevel at $\theta = \pi/4$ parallels the behavior of the integrated intensity in Figure 6B. Figure 9D shows that the level crossings that are apparent at $\theta = 0$ (Figure 9A) are forbidden due to the presence of off-diagonal terms in the spin-Hamiltonian. The behavior of the total MCD intensity shown in Figure 9C can nevertheless be understood from the fact that the wave function describing the lowest sublevel is still allowed to change with magnetic field. Thus there is a gradual change of the lowest sublevel from a $M_S = -{}^1/_2$ level quantized along the molecular z-axis to a $M_S = -{}^5/_2$ level quantized along the applied field. Since this change is rather slow, saturation is not observed over the range $\beta B/2kT = 0-1.56$ that is commonly experimentally accessible.

In summary, in systems with intermediate ZFS both (avoided) level crossing and off-axis effects are of dominant importance. For $D < 0$ the behavior is dominated by the off-axis behavior of the lowest energy sublevel that is classified as "$M_S = -S$" over the entire magnetic field range while for $D > 0$ the behavior contains contributions from various sublevels that show avoided crossing which results in a strong change in the character of the ground state sublevel wave function with increasing magnetic field.

Finally, Figure 10 shows the behavior of the saturation magnetization curves with changing magnitude of D in the intermediate regime for both $D < 0$ (Figure 10A) and $D > 0$ (Figure 10B). The strong dependence of the shape of the saturation magnetization behavior on the sign and magnitude of D demonstrates that determination of the sign and magnitude of D from MCD is feasible in the intermediate regime.[56] The behavior of systems in the intermediate ZFS regime is complicated, however, and requires numerical simulations to analyze experimental data. In general, the saturation magnetization

(56) Note that the saturation magnetization curves of systems with positive D are more sensitive to the magnitude of D because the components with smaller $|M_S|$ that are associated with smaller effective g-values are lowest in energy at small magnetic fields.

behavior will be sensitive to all parameters, the sign and magnitude of *D*, *E/D*, and the transition polarizations.

3.2. *C*-Term Signs from Molecular Wave Functions. In this section the prediction of *C*-term signs from molecular orbital calculations is discussed. The linear regime of the MCD *C*-term response is employed because in this case the integrations in eq 2 can be performed analytically. In section 3.2.1 the theory is developed for $S = {}^1/_2$ systems and in 3.2.2 for a general Kramers system with either large or very small ZFS. To show the application of the expressions derived in 3.2.1 and 3.2.2, two examples from the literature are briefly treated in 3.2.3. In 3.2.3.A the dominant *C*-terms exhibited by the biological Cu_A electron transfer center are analyzed, and in 3.2.3.B an analogous analysis is presented for the high-spin ferric complex $[Fe(EDTA)(O_2)]^{3-}$. These two molecules are chosen to (1) apply the methodology to systems that are well understood and (2) show the physical insight that can be obtained into the origin of *C*-term signs from qualitative arguments.

3.2.1. $S = {}^1/_2$ Systems. For the prediction of *C*-term signs it is convenient to take the linear limit of eq 36 that followed from eq 26 and perform the average over all angles, giving eq 42,

$$\frac{\Delta\epsilon}{E} = -\gamma\frac{\beta_B B}{2kT}\left\{\frac{1}{3}[M_{yz}^{\mathrm{eff}} g_x + M_{xz}^{\mathrm{eff}} g_y + M_{xy}^{\mathrm{eff}} g_z]\right\} \qquad (42)$$

where the expression in curly brackets is identified as the $\bar{C}_0$-parameter. Expressing the effective transition dipole moment products in terms of transition dipole and reduced SOC matrix elements, eq 37, $\bar{C}_0$ in eq 1 is given by

$$\bar{C}_0 = -{}^1/_6\sum_{u\upsilon w}\epsilon_{u\upsilon w} g_w \sum_{K\neq A,J}\{\Delta_{KJ}^{-1}\,\vec{D}_u^{KA}\,\vec{D}_\upsilon^{AJ}\,\bar{L}_w^{KJ} + \Delta_{KA}^{-1}\,\vec{D}_u^{AJ}\,\vec{D}_\upsilon^{JK}\,\bar{L}_w^{KA}\} \qquad (43)$$

where $\epsilon_{u\upsilon w}$ is the Levi−Civitta symbol ($u,\upsilon,w = x,y,z$). Using the matrix elements in Tables 1 and 2, eq 43 takes the form given in eq 44. Equation 44a applies to transitions from a doubly occupied MO ψ_o (state I_i^o) and eq 44b to the promotion of the unpaired electron in ψ_o into an empty MO ψ_a (state II_o^a).

$$\bar{C}_0(I_i^o) = -\frac{1}{12}\sum_{\substack{j\neq i\\ \text{doubly}}}\sum_{u\upsilon w}\epsilon_{u\upsilon w} g_w\{\Delta_{I_j^o A}^{-1}\,\mathrm{Im}\langle\psi_o|\textstyle\sum_N\xi(r_N)\vec{l}_{N,w}|\psi_j\rangle \times \langle\psi_i|\vec{r}_u|\psi_o\rangle\langle\psi_j|\vec{r}_\upsilon|\psi_i\rangle + \Delta_{I_j^o I_i^o}^{-1}\,\mathrm{Im}\langle\psi_i|\textstyle\sum_N\xi(r_N)\vec{l}_{N,w}|\psi_j\rangle \times \langle\psi_o|\vec{r}_u|\psi_j\rangle\langle\psi_i|\vec{r}_\upsilon|\psi_o\rangle\} \qquad (44a)$$

$$\bar{C}_0(II_o^a) = -\frac{1}{12}\sum_{\substack{b\neq a\\ \text{empty}}}\sum_{u\upsilon w}\epsilon_{u\upsilon w} g_w\{\Delta_{II_o^b}^{-1}\,\mathrm{Im}\langle\psi_b|\textstyle\sum_N\xi(r_N)\vec{l}_{N,w}|\psi_o\rangle \times \langle\psi_o|\vec{r}_u|\psi_a\rangle\langle\psi_b|\vec{r}_\upsilon|\psi_o\rangle + \Delta_{II_o^b I_o^a}^{-1}\,\mathrm{Im}\langle\psi_b|\textstyle\sum_N\xi(r_N)\vec{l}_{N,w}|\psi_a\rangle \times \langle\psi_o|\vec{r}_u|\psi_b\rangle\langle\psi_a|\vec{r}_\upsilon|\psi_o\rangle\} \qquad (44b)$$

The result obtained is similar to that of Gerstman and Brill[17] (their eq 28a) but has the advantage that it has been derived from a many electron picture and uses the more general SOC operator in eq 8. Further, eqs 44a,b use MO wave functions rather than hybrid atomic orbitals, which is more realistic. Note that the energy denominators used here refer to state energies and not orbital energies. Thus $\Delta_{I_j^o A}^{-1}$ is a positive quantity although ψ_j is lower in energy than ψ_o. Also the one-electron SOC constants obtained by evaluating the one-center radial parts of the matrix elements of the reduced SOC operator are inherently positive. This differs from the usual practice followed in ligand field treatments that is to use the atomic many electron SOC constants λ.

It is interesting to note that application of eqs 44a and 44b to d^1 and d^9 systems predicts oppositely signed *C*-terms for comparable transitions in these systems. In the case of d^9 systems the transitions usually observed are into the singly occupied MO, ψ_o, while in the d^1 systems at least the d−d transitions are from the half-occupied MO into empty MOs. The sign change occurs from the reversed order of the perturbing MOs (ψ_j and ψ_b) in the matrix elements of the reduced SOC operator in eq 44a relative to eq 44b.

3.2.2. High-Spin System. Application to $S = 5/2$. In the case of strong ZFS, it is convenient to follow an analogous procedure and derive the MCD *C*-term response of the $(2S + 1)/2$ Kramers doublets of the ground state configuration in the linear limit. The dominance of the ZFS suggests the use of the eigenfunctions of $H_{\mathrm{BO}} + H_{\mathrm{ZFS}}$ as field independent basis and then the use of first order degenerate perturbation theory to construct the field dependent states. The energies of the two components of the *d*th doublet in the presence of the ZFS and Zeeman interactions are given by

$$E_\pm^{(d)} = E^{(d)} \pm {}^1/_2\tilde{g}^{(d)}\beta_B B \qquad (45)$$

where $E^{(d)}$ is the energy of the *d*th doublet at zero magnetic field. $\tilde{g}^{(d)}$ is calculated from the effective *g*-values of the *d*th doublet in analogy to the true $S = {}^1/_2$ case:

$$\tilde{g}^{(d)} = \sqrt{(\tilde{g}_x^{(d)} l_x)^2 + (\tilde{g}_y^{(d)} l_y)^2 + (\tilde{g}_z^{(d)} l_z)^2} \qquad (46)$$

From this the Boltzmann populations are evaluated to first order in the applied field:

$$N_\pm^{(d)} = {}^1/_2\alpha_d(1 \mp {}^1/_2\tilde{g}\beta_B B/kT) \qquad (47)$$

where

$$\alpha_d = \frac{\exp(-E^{(d)}/kT)}{\sum_s \exp(-E^{(s)}/kT)} \qquad (48)$$

The pseudo $S = {}^1/_2$ spin expectation values become

$$\langle\tilde{\vec{S}}\rangle_\pm^{(d)} = \pm\frac{1}{2\tilde{g}^{(d)}}(\tilde{g}_x^{(d)} l_x, \tilde{g}_y^{(d)} l_y, \tilde{g}_z^{(d)} l_z) \qquad (49)$$

and eq 26 assumes the form

$$\frac{\Delta\epsilon}{E} = \gamma\sum_d \alpha_d\frac{\beta_B B}{kT}\bar{C}_0^{(d)} \qquad (50a)$$

with

$$\bar{C}_0^{(d)} = -\frac{1}{12S}(\tilde{g}_x^{(d)} M_{yz}^{\mathrm{eff}} + \tilde{g}_y^{(d)} M_{xz}^{\mathrm{eff}} + \tilde{g}_z^{(d)} M_{xy}^{\mathrm{eff}}) \qquad (50b)$$

Note that eq 50 properly reduces to the $S = {}^1/_2$ case if there is only one doublet and therefore the effective and real *g*-values coincide. Equation 50 may be interpreted as a generalization of the *C*-term part of eq 1 for the high-spin case and also defines

Table 4. The MCD Spectrum Displayed by the Cu_A Electron Transfer Site, Assignments in the Idealized Point Group D_{2h} from Refs 21 and 57, Predicted Polarizations, and Predicted *C*-Term Signs Based on Eq 44a and Figure 11

band	energy (cm^{-1})	assignment exc state	assignment transition	pol	*C*-term sign obsd	*C*-term sign predicted	ref
6	19 000	^2A_g	$a_g \rightarrow b_{3u}$	X	+	+	21
		$^2B_{1g}$	$b_{1g} \rightarrow b_{3u}$	Y	+	+	57
7	21 000	$^2B_{1g}$	$b_{1g} \rightarrow b_{3u}$	Y	−	−	21
		^2A_g	$a_g \rightarrow b_{3u}$	X	−	−	57

Table 5. The MCD Spectrum Displayed by $[Fe(EDTA)(O_2)]^{3-}$, Assignments in the Idealized Point Group C_{2v} from Ref 30, Predicted Polarizations, and Predicted *C*-Term Signs Based on Eqs 51 and 37 and Figure 12

band	energy (cm^{-1})	assignment exc state	assignment transition	pol	*C*-term sign obsd	*C*-term sign predicted
3	18 800	$^6A_1^a$	$\pi^* \rightarrow yz$	X	+	+
4	21 700	$^6B_1^a$	$\pi^* \rightarrow xz$	Y	−	−

the *c*-coefficients in eq 39 used by Browett et al.[24a] Note that the $\bar{C}_0^{(d)}$'s are of the same sign for each doublet. Equation 50 allows one not only to compute the relative contributions from each doublet to the total MCD *C*-term intensity but also to predict the overall sign through evaluation of the effective transition moment products from electronic structure calculations using eq 37. For the case of MO wave functions the matrix elements required to evaluate eq 50 are given in Tables 1 and 2. For weak and intermediate ZFS, a convenient method is to calculate the *C*-term signs in the saturation limit, i.e., for very low temperature and very high fields. In this case only the lowest Zeeman sublevel is populated and, if the real *g*-matrix is isotropic, has a spin expectation value $-S$ in the direction of the applied field. Inserting $N_1 = 1$ and $\langle \vec{S} \rangle_1 = -\vec{l}S$ into eq 26 and performing the integrations gives

$$\frac{\Delta\epsilon}{E} = -\frac{1}{3}\gamma\{M_{xy}^{\text{eff}} + M_{xz}^{\text{eff}} + M_{yz}^{\text{eff}}\} \qquad (51)$$

Note that in this limit eq 51 shows that the MCD becomes independent of field, temperature, and effective *g*-values, as required. Thus, direct application of eq 37 with the matrix elements given in Tables 1 and 2 permits one to predict the sign of the MCD *C*-term in the saturation limit.

3.2.3. Examples. A. $S = {}^1/_2$ Example. As an example of the application of eq 44 we will briefly comment on the dominant *C*-terms displayed by the binuclear, dithiolate-bridged mixed-valence copper center ([Cu(1.5)...Cu(1.5)], $S = {}^1/_2$) known as Cu_A and discussed in detail in refs 21, 57, and 20. The MCD spectrum in the visible region consists of a very intense pseudo-*A* pair of *C*-terms with components centered around 19 000 (positive) and 21 000 cm^{-1} (negative) ($\Delta\epsilon \approx 1800$ M^{-1} cm^{-1} at 4 T). The orbital nature of these transitions is well understood and summarized in Table 4.[21,57] The main contribution to the *C*-term intensity arises from the SOC between excited states (second term in { }, eq 44a), that is very effective due to the close energetic proximity and orthogonal polarization of the transitions involved.[21,57]

In this case eq 44a can be applied in a graphical form that is illustrated in Figure 11. Figure 11A shows the four core atoms of the Cu_A chromophore. Figure 11B shows the donor MO ψ_i and intermediate MO ψ_j involved in the transition of interest

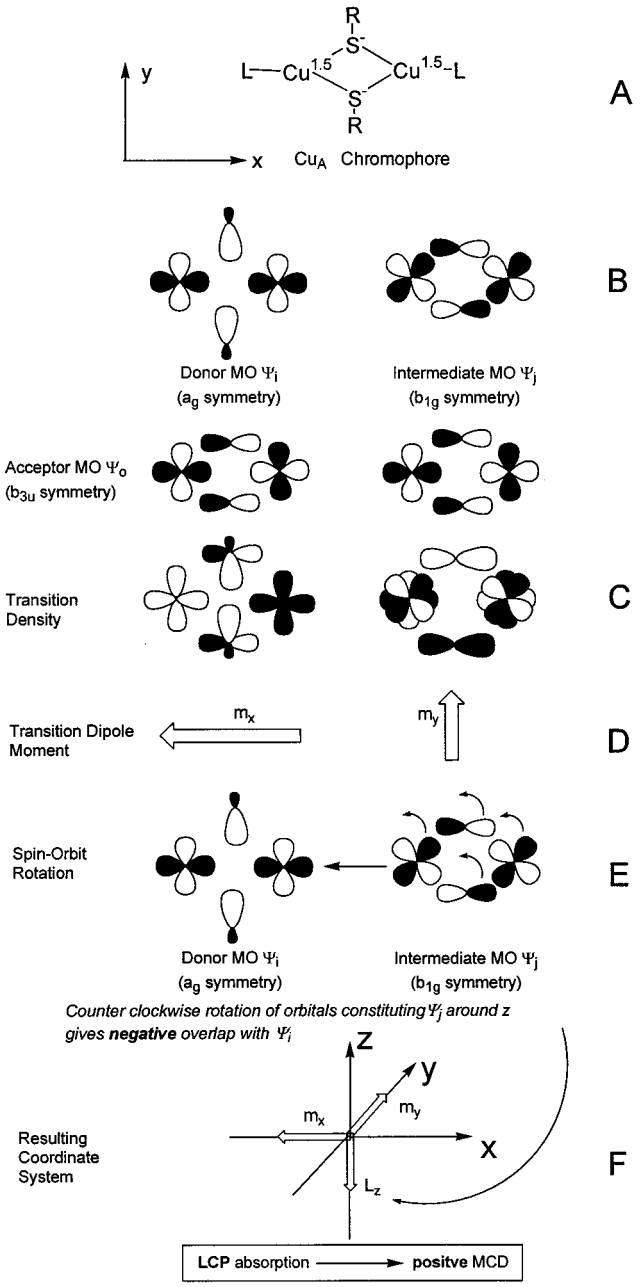

Figure 11. Graphical prediction of the *C*-term sign for the $a_g \rightarrow b_{3u}$ transition observed at 19 000 cm^{-1} in the Cu_A electron transfer center. (A) Structure of the chromophore and choice of coordinate axes. (B) The donor MO ψ_i (a_g; left) and the intermediate MO ψ_j (b_{1g}; right) of eq 44a). (C) The transition densities for the transitions $a_g \rightarrow b_{3u}$ and $b_{1g} \rightarrow b_{3u}$. (D) Direction of the transition dipole moments for the two transitions. (E) Graphical determination of the sign of the reduced spin−orbit coupling matrix element between the two excited states. (F) Coordinate system showing that the transition dipole moment and reduced spin−orbit vectors form a right-handed system.

(44a). The product of the donor and acceptor MOs and the intermediate and acceptor MOs are shown in Figure 11C and define the respective transition densities.[32] The dipole moments of the charge distributions in Figure 11C are given in Figure 11D and define the transition dipole moments pointing along $-x$ and $+y$, respectively.[58] In order to evaluate eq 44a, the spin-

(57) Gamelin, D. R.; Randall, D. W.; Hay, M. T.; Houser, R. P.; Mulder, T. C.; Canters, G. W. de Vries, S.; Tolman, W. B.; Lu, Y.; Solomon, E. I. *J. Am. Chem. Soc.* **1998**, *120*, 5246.

(58) The transition dipole moment is defined to point from the center of negative charge (black) to the center of positive charge (white). Note that this definition does not influence the prediction of *C*-term signs since a product of two transition dipole moments is involved.

orbit rotation of the intermediate MO ψ_j into the donor MO ψ_i is shown in Figure 11E and is seen to lead to a negative reduced SOC matrix element.[59] This defines a vector perpendicular to the plane of orbital rotation that points along $-z$. Thus one can evaluate the sign of the second term in eq 44a as follows:

$$\bar{C}_0(a_g \rightarrow b_{3u}) \propto (-1)\sum_{uvw} \epsilon_{uvw}\Delta^{-1} g_w \,\mathrm{Im}\langle a_g|\sum_A \xi(r_A) l_{A,w}|b_{1g}\rangle \times \langle b_{3u}|\vec{r}_u|b_{1g}\rangle\langle a_g|\vec{r}_v|b_{3u}\rangle \propto (-1)\Delta^{-1} g_z \begin{pmatrix} 0 \\ 0 \\ -|\bar{L}_z| \end{pmatrix}\left\{\begin{pmatrix} 0 \\ +|m_y| \\ 0 \end{pmatrix}\times \begin{pmatrix} -|m_x| \\ 0 \\ 0 \end{pmatrix}\right\} \propto (-1)\Delta^{-1} g_z(-|\bar{L}_z|)(-(|m_y|)(-|m_x|)) \propto +\Delta^{-1} g_z \tag{52}$$

where $\Delta = E(b_{1g} \rightarrow b_{3u}) - E(a_g \rightarrow b_{3u})$. Altogether the three vectors are seen to define a right-handed coordinate system, Figure 11F, which means that for positive Δ this mechanism will lead to absorption of left-handed photons. By means of eq 3 this defines a positive MCD signal. By the nature of the pseudo-*A* mechanism,[4,5,17] the $b_{1g} \rightarrow b_{3u}$ *C*-term is proportional to $-\Delta^{-1}$. Thus, independent of the relative order of the two states, one expects the higher energy band to have a negative MCD *C*-term and the lower one to be positive, consistent with experiment (Table 4).

B. $S = {}^5/_2$ Example. To illustrate the analogous procedure for high-spin systems, the MCD *C*-terms displayed by the high-spin ferric complex $[Fe(EDTA)(O_2)]^{3-}$ are analyzed. In a recent study it was shown to have $D = -1 \pm 0.25$ cm^{-1} and $E/D = 0.21$.[30] For this case only the lowest Kramers doublet is populated at 1.5 K and 7 T magnetic field and therefore eq 51 applies. The effective chromophore symmetry is C_{2v}, and the ground state is designated $^6A_1^{g.s.}$. The complex displays an absorption band centered around 20 000 cm^{-1} that is associated with a pair of oppositely signed *C*-terms (Table 5). The assignment of this spectrum shows that the pair of transitions is due to peroxide $\rightarrow$ Fe LMCT originating from a doubly occupied peroxide π^* orbital into the half-occupied Fe-*yz* and Fe-*xz* based MOs (Table 5). Since $^6A_1^{g.s.}$ is energetically well separated from the sextet-CT manifold, the MCD intensity must arise from SOC between the two excited states, $^6A_1^a(\pi^* \rightarrow yz)$ and $^6B_1^a(\pi^* \rightarrow xz)$, that is allowed via the *z*-component of the SOC operator (i.e., the $l_{Fe,z}$ operator rotates *xz* into *yz*). Using eqs 51 and 37, one has for the MCD intensity of the transition $^6A_1^{g.s.} \rightarrow {}^6A_1^a(\pi^* \rightarrow yz)$

$$\frac{\Delta\epsilon}{E} = +\frac{\gamma}{3}\frac{\mathrm{Im}\langle {}^6B_1^a\,{}^5/_2|\sum_{N,i}\xi(r_{iN})\, l_{N,z}(i)\, s_0(i)|{}^6A_1^a\,{}^5/_2\rangle}{E({}^6B_1^a) - E({}^6A_1^a)} \times \langle {}^6B_1^a\,{}^5/_2|m_y|{}^6A_1^{g.s.}\,{}^5/_2\rangle\langle {}^6A_1^{g.s.}\,{}^5/_2|m_x|{}^6A_1^a\,{}^5/_2\rangle$$

and the negative of this for the transition $^6A_1^{g.s.} \rightarrow {}^6B_1^a(\pi^* \rightarrow xz)$. This situation is graphically illustrated in Figure 12. The two transition dipole moments are pointing along $-x$ and $+y$, respectively, and the spin−orbit rotation leads to a negative reduced SOC matrix element. Since $^6B_1^a(\pi^* \rightarrow xz)$ is higher in energy than $^6A_1^a(\pi^* \rightarrow yz)$, the denominator is positive and a positive *C*-term is predicted for the lower energy band and a negative one for the higher energy band which is also observed experimentally (Table 5).

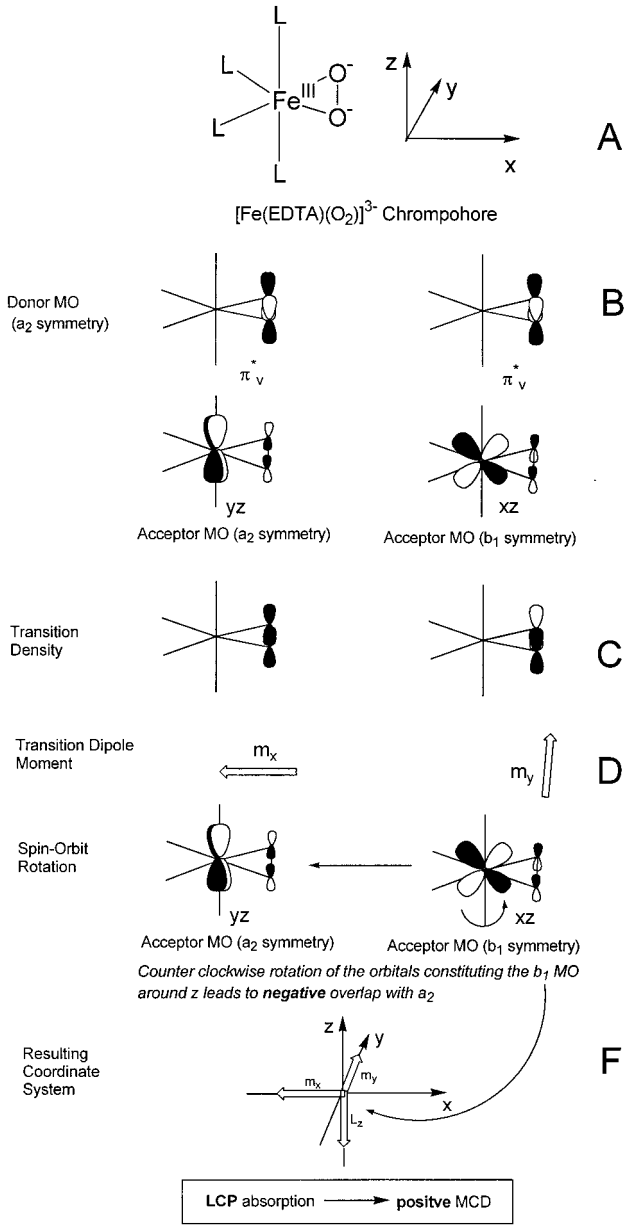

Figure 12. Graphical prediction of the *C*-term sign for the $^6A_1^{g.s.} \rightarrow {}^6A_1^a(\pi^* \rightarrow yz)$ transition of the complex $[Fe(EDTA)(O_2)]^{3-}$. (A) Structure of the chromophore and choice of coordinate axes. (B) The donor MO and the acceptor MOs involved in the transitions $^6A_1^{g.s.} \rightarrow {}^6A_1^a(\pi^* \rightarrow yz)$ (left) and $^6A_1^{g.s.} \rightarrow {}^6B_1^a(\pi^* \rightarrow xz)$ (right). (C) The transition densities of the two transitions. (D) The transition dipole moments for the two transitions. (E) Graphical determination of the sign of the reduced spin−orbit coupling matrix element between the two excited states. (F) Coordinate system showing that the transition dipole moment and reduced spin−orbit vectors form a right-handed system.

The results of 3.2.3.A,B illustrated a general feature of pseudo-*A* terms in low-symmetry systems, namely, that switching the order of the excited states does not lead to an oppositely signed pseudo-*A* term because changing the order of the two states also changes the sign of the relevant energy denominator. However, the fact that the lower energy component happened

(59) The rotation is defined such that if one views down the rotation axis each basis orbital in the MO to the right (ψ_j here) is to be rotated counterclockwise. Neglect of multicenter integrals in the evaluation of the reduced spin−orbit coupling operator means that each basis orbital is only rotated by the angular momentum operator that is attached to the same center.

to be positive in both examples is not a general result. In general, each contribution to a *C*-term sign involves products of three matrix elements (eq 37), that all can be of either sign. The overall sign is determined by the transition dipole moment directions and reduced SOC matrix elements. These quantities depend on the spatial symmetries of the wave functions or, in MO approximation, on the shapes of the MOs involved in the transition and intermediate states in a way shown in the preceding two paragraphs. This also means that the symmetry of a given excited state does not determine its *C*-term sign in low-symmetry systems. Thus, sign predictions are more difficult than in high-symmetry systems where the ground and excited state symmetries alone determine the *C*-term signs.

4. Discussion

In this study spin−orbit coupling contributions to MCD *C*-term signs and saturation behavior for a transition between two orbitally nondegenerate manifolds *A* and *J* has been evaluated. The key results are eqs 21−23 and 26; all equations developed in section 3 follow from these expressions. The model presented contains a number of previous treatments as special cases and also provides new insight: (1) It is valid for any ground state spin *S*, any relative orientation of magnetic coupling tensors, and the general case of arbitrary transition polarization. (2) The theory relates the contributions of the individual ground state sublevels to the total MCD intensity in a rigorous way through their spin-expectation values and therefore considerably reduces the number of parameters required to analyze experimental data. For systems with an odd number of electrons it follows that the relative contributions of the different Kramers doublets to the total MCD intensity are proportional to their effective *g*-values. (3) The model is valid for the entire range of relative magnitudes of Zeeman and ZFS and therefore allows the analysis of VTVH-MCD data regardless of level crossings. (4) It can be used to calculate *C*-term signs from molecular wave functions.

4.1. Saturation Magnetization. The generalization to any *S* is useful from a conceptual point of view because it shows the underlying consistency for all systems and leads to general rules. From a practical point of view eqs 21−23, 26, 36, and 50, which describe the magnetization behavior, make no assumptions about the symmetry of magnetic coupling tensors or transition polarizations. This is potentially important in the analysis of low-symmetry systems. To illustrate the possible effects, Figure 13 shows the saturation magnetization curves computed for a hypothetical $S = {}^5/_2$ system with $D = +3.5$ cm^{-1} and intermediate rhombicity ($E/D = 0.12$). In Figure 13A a simulation is shown with the frequently invoked axial approximation $M_{xz} = M_{yz}$. Figure 13B allows for $M_{xz} \neq M_{yz}$ and shows that the changes in the computed saturation curves are minimal if M_{xz} and M_{yz} are of the same sign. However, qualitatively different shapes for the saturation curves are obtained if the contributions from M_{xz} and M_{yz} oppose each other as shown in Figure 13C. On the basis of eqs 21−23 this is not an unrealistic situation,[60] and the dramatic difference between the computed curves underlines the need to utilize expressions for the general case.

An important aspect of MCD spectroscopy is that, like ENDOR spectroscopy, it is orientation selective, which means that only a subset of suitably oriented molecules contribute to the MCD signal. Thus the analysis of MCD magnetization

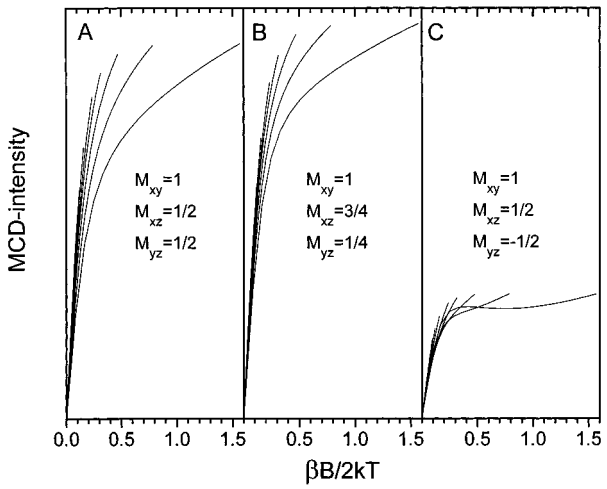

Figure 13. Effect of nonaxial polarization on MCD saturation magnetization curves for a hypothetical system with $D = +3.5$ cm^{-1} and $E/D = 0.12$. Isotherms were calculated at 1.5, 3, 5, 7.5, 10, 15, 20, and 25 K for 20 field values between 0 and 7 T. (A) Saturation magnetization curves for axial polarization. (B) Effect of introducing nonaxial polarization with M_{xz} and M_{yz} of the same sign. (C) Effect of introducing nonaxial polarization with M_{xz} and M_{yz} of different sign.

curves allows orientation information to be obtained from samples of randomly oriented molecules through the transition polarizations. For example, a strongly allowed LMCT band will be polarized along the metal−ligand bond. Therefore assignment of CT bands to specific ligands based on the analysis of MCD saturation magnetization curves is feasible.

It must be stressed that the coordinate system that the theoretical polarizations refer to are determined by the underlying spin-Hamiltonian that is diagonalized to obtain the spin-expectation values in eq 26. Frequently it will be convenient to choose the coordinate system that diagonalizes the **D**-tensor or the **g**-matrix (for $S = {}^1/_2$). The magnetic coupling tensors can be rotated into another convenient coordinate system, for example, one that is chosen on the basis of the knowledge of transition polarizations in a suitable molecular frame. If the principal axis system of a magnetic coupling tensor is chosen as reference coordinate system, it is important to know the orientation of this tensor in the molecular framework from either theory or experiment if the theoretical polarizations are to be interpreted in terms of a molecular axis system.

Another aspect of the theory is that it relates the contributions of different Kramers doublets to the total MCD signal. One of the important results from this study is the fact that the connection is simply provided by the spin-expectation values of the magnetic ground state sublevels. These are conveniently generated from the solution of a SH eigenvalue problem. As shown in sections 3.1.3.A and 3.2.2, the contribution of each Kramers doublet to the total MCD intensity is proportional to the effective *g*-value of this doublet that is orthogonal to the plane of polarization (eq 50). Therefore the relative contributions can be fixed from theory, which should be beneficial for the analysis of ZFSs from MCD spectroscopy. For the analysis of MCD data for Kramers systems with large ZFSs in the linear region, eq 50 can be used in the form

$$\frac{\Delta\epsilon}{E} = A_{\text{satlim}}\left\{\left[\sum_d \alpha_d \frac{\beta B}{kT}(\tilde{g}_x^{(d)} M_{yz}^{\text{eff}} + \tilde{g}_y^{(d)} M_{xz}^{\text{eff}} + \tilde{g}_z^{(d)} M_{xy}^{\text{eff}})\right] + xB\right\} \quad (53)$$

(60) For example consider eq 22 and $\vec{D}^{KA} \propto (1,1,0)$ and $\vec{D}^{AJ} \propto (0,1,-{}^1/_2)$ leading to $M_{xy} \propto 1$, $M_{xz} \propto {}^1/_2$, and $M_{yz} \propto -{}^1/_2$.

where α_d is the fractional population of the dth Kramers doublet at zero field that depends on the ZFS parameters, $\tilde{g}^{(d)}_{x,y,z}$ are the effective g-values of the dth Kramers doublet, A_{satlim} is a scaling parameter, and the M's are the effective transition dipole products. The term $A_{\text{satlim}}xB$ is added in an ad hoc fashion to describe possible B-term contributions in an average way.[24a]

Since the spin-expectation values required to evaluate eq 26 can be generated from an eigenvalue problem, there is no problem with the possible divergence of a perturbation sum. Thus, the theory remains valid in the important case that the ground state magnetic sublevels cross as a function of magnetic field. With present instrumentation, magnetic fields of $\approx$7 T corresponding to Zeeman energies on the order of $\approx$10 cm^{-1} are used in routine measurements. Since many of the systems that are of interest have ZFSs $\leq$10 cm^{-1}, level crossings are the rule rather than the exception in MCD experiments. For these systems increasing magnetic field changes the quantization axis of the electron spin from being internally quantized (by the ZFS along the molecular z-axis) to being externally quantized (by the applied magnetic field along the laboratory z-axis). The behavior of the spin-expectation values in such cases is in general very complicated and cannot be derived analytically. Thus, one has to rely on numerical simulations in order to exploit the whole experimentally accessible B/T space in the analysis. In section 3.1.3.C it was found that off-axis contributions make dominant contributions to the MCD saturation magnetization for systems with $D < 0$ and avoided crossings determine the behavior of systems with $D > 0$. In general the saturation magnetization curves of systems with intermediate ZFS (relative to the Zeeman energy) depend on all of the magnetic coupling parameters (sign and magnitude of D, E/D) and the transition polarizations and are thus potentially most informative. The D-values extracted from MCD experiments will frequently be reliable for the sign and magnitude of D, but will not be highly accurate.

In the limit of zero ZFS it was shown in section 3.1.3.B that the MCD saturation magnetization curves coincide with the Brillouin functions for spin S. In this case nesting of isotherms is not observed and the only information that is deducible from MCD saturation studies is the value of the total spin S. However, the absence of nesting does not require the presence of small ZFS, because it also occurs for $S > {}^1/_2$ systems with large ZFSs and polarizations orthogonal to directions with large effective g-values as shown in Figure 2. In this case the use of Brillouin functions to determine the ground state spin is misleading and an approach based on fitting the magnetization curves to an effective $S = {}^1/_2$ model and inferring the spin state from the effective g-value returned by the fit appears most promising. In any case, the observation of nesting in the isotherms is indicative of a situation where neither a Brillouin function nor an effective g-value approach is appropriate.

4.2. Selection Rules. The three key mechanisms that lead to MCD intensity by means of SOC are described by eqs 21−23. Equation 21 is a two-state mechanism that shows that the MCD C-term intensity induced by SOC between states A and J is proportional to the cross product of the transition dipole moment for the $A \rightarrow J$ transition with the difference in dipole moments of states A and J. The group theoretical selection rules contained in eq 21 require that the transition $A \rightarrow J$ is allowed, i.e., the direct product $\Gamma_A \otimes \Gamma_{x,y,z} \otimes \Gamma_J$ must contain the totally symmetric representation. In order for a dipole moment to be present in either the ground or excited state, at least one of the components of the dipole operator must transform as the totally symmetric representation if both A and J are spatially nondegenerate. However, the change of dipole moment will most likely be in the direction in which charge is displaced during the transition and the mechansim in eq 21 will produce only minor MCD C-term intensity.

Equation 22 describes a three-state mechanism for MCD C-term intensity. Here an intermediate state K spin−orbit couples with the excited state J. In this way the transition $A \rightarrow J$ acquires some character of the transition $A \rightarrow K$ and given that the transition moment of $A \rightarrow K$ is not collinear with that of $A \rightarrow J$ provides the orthogonal polarization required for MCD intensity. Equation 22 leads to the rule that the sum over all transitions induced by this mechanism is zero because $\Delta^{-1}_{KJ} = -\Delta^{-1}_{JK}$, $\bar{L}^{KJ} = -\bar{L}_{JK}$, and $(D^{\text{AK}} \times \vec{D}^{\text{AJ}}) = -(\vec{D}_{AJ} \times \vec{D}_{AK})$. This result has been shown before by Gerstman and Brill for a $S = {}^1/_2$ system.[17] For a state K in eq 22 to give a nonvanishing contribution the constraints from group theory are

$$\Gamma_A \otimes \Gamma_{x,y,z} \otimes \Gamma_J = A_{1g} \tag{54a}$$

$$\Gamma_A \otimes \Gamma_{x,y,z} \otimes \Gamma_K = A_{1g} \tag{54b}$$

$$\Gamma_J \otimes \Gamma_{Rx,Ry,Rz} \otimes \Gamma_K = A_{1g} \tag{54c}$$

If the symmetry group of the molecule contains a center of inversion, this means that states J and K must be of like parity and of opposite parity to the ground state.

Equation 23 is also a three-state mechanism. Here an intermediate state K spin−orbit couples with the ground state. In this way the transition $A \rightarrow J$ acquires some character of the "virtual" transition $K \rightarrow J$. If the transition moment of $K \rightarrow J$ is not zero and not collinear with that of $A \rightarrow J$, this will induce MCD intensity. As noted before,[17] it is this mechanism that leads to deviations from the sum rule described in the previous paragraph that are frequently observed experimentally. The group theoretical selection rules for this mechanism require

$$\Gamma_A \otimes \Gamma_{x,y,z} \otimes \Gamma_J = A_{1g} \tag{55a}$$

$$\Gamma_J \otimes \Gamma_{x,y,z} \otimes \Gamma_K = A_{1g} \tag{55b}$$

$$\Gamma_A \otimes \Gamma_{Rx,Ry,Rz} \otimes \Gamma_K = A_{1g} \tag{55c}$$

Thus, in the presence of a center of inversion, K must have the same parity as the ground state that is opposite of state J.

4.3. *C*-Term Signs. The model also leads to explicit expressions for computing MCD C-term signs from molecular wave functions through eqs 37, 44, 50, and 51. Thus, these expressions can be used to facilitate band assignments and to get insight into excited state properties. While in the general case first-order perturbation theory will not be accurate to treat the SOC because there will almost always be excited state near degeneracies, it gives insight into the nature of the problem and provides a basis for qualitative arguments. Thus, the C-term signs are determined by the transition densities (describing displacement of charge in the transition) and reduced SOC matrix elements (describing rotations of charge induced by SOC). In sections 3.2.3.A,B two examples were provided for pseudo-A terms displayed by the biological Cu_A ($S = {}^1/_2$) electron transfer center and the $[Fe(EDTA)(O_2)]^{3-}$ ($S = {}^5/_2$) complex, and it was shown that the C-term sign for a given transition can be determined by a graphical method. In the case of pseudo-A terms, the excited state SOC, eq 22, is the main contributor to MCD C-term intensity. Importantly, the sign of the pseudo-A feature does not depend on the specific order of the two excited states because changing the order also changes the C-term sign for both transitions through the energy denominator in eq 22. Thus,

in low-symmetry systems, the excited state symmetry does not uniquely determine the *C*-term sign of spin-allowed transitions as is the case for high-symmetry systems, where all important SOC occurs within the orbitally degenerate ground or excited state manifolds.

In summary, a model has been developed to predict saturation magnetization curves and *C*-term signs measured in MCD experiments and applied to the case of $S = {}^1/_2$ and $S = {}^5/_2$ systems. The results enable the determination of transition polarizations and magnetic coupling parameters from samples of randomly oriented molecules using the entire available VTVH-MCD experimental information. Finally, it is noted that the application of the theory developed here is not restricted to monomeric transition metal complexes. Together with a suitable spin-Hamiltonian, exchange coupled oligomeric species can also be treated. Applications along these lines are in progress.

Acknowledgment. Our research is supported by the National Institutes of Health (GM40392). F.N. thanks the Deutsche Forschungsgemeinschaft for a postdoctoral fellowship and Dr. Thomas Brunold for careful reading of the manuscript.

Note Added in Proof. Most recently an alternative treatment of spin−orbit coupling contributions to MCD intensities for systems with $S > {}^1/_2$ has appeared[61] which emphasizes the use of point group coupling coefficients.

Supporting Information Available: Derivation of eq 17 and library of simulated magnetization curves for $S = {}^5/_2$. This material is available free of charge via the Internet at http://pubs.acs.org.

IC981264D

(61) Oganesyan, V. S.; George, S. J.; Cheesman, M. R.; Thomson, A. J. *J. Chem. Phys.* **1999**, *110*, 762−777.